TOWARD SINGLE-MOLECULE DNA UPTAKE BY *HAEMOPHILUS INFLUENZAE*

by

Philip J. M. Johnson
B.Sc. (Honours), Memorial University of Newfoundland, 2004

THESIS SUBMITTED IN PARTIAL FULFILLMENT
OF THE REQUIREMENTS FOR THE DEGREE OF
MASTER OF SCIENCE
IN THE DEPARTMENT
OF
PHYSICS

SIMON FRASER UNIVERSITY
Summer 2007

APPROVAL

Name:	Philip J. M. Johnson
Degree:	Master of Science
Title of Thesis:	Toward single-molecule DNA uptake by *Haemophilus influenzae*
Examining Committee:	Dr. Karen Kavanagh (Chair)
	Dr. Nancy R. Forde (Senior Supervisor)
	Dr. Eldon Emberly (Supervisor)
	Dr. John Bechhoefer (Supervisor)
	Dr. Edgar Young (Supervisor)
	Dr. Jenifer Thewalt (Internal Examiner)
Date Approved:	April 26 2007

SFU SIMON FRASER UNIVERSITY
LIBRARY

Declaration of Partial Copyright Licence

The author, whose copyright is declared on the title page of this work, has granted to Simon Fraser University the right to lend this thesis, project or extended essay to users of the Simon Fraser University Library, and to make partial or single copies only for such users or in response to a request from the library of any other university, or other educational institution, on its own behalf or for one of its users.

The author has further granted permission to Simon Fraser University to keep or make a digital copy for use in its circulating collection (currently available to the public at the "Institutional Repository" link of the SFU Library website <www.lib.sfu.ca> at: <http://ir.lib.sfu.ca/handle/1892/112>) and, without changing the content, to translate the thesis/project or extended essays, if technically possible, to any medium or format for the purpose of preservation of the digital work.

The author has further agreed that permission for multiple copying of this work for scholarly purposes may be granted by either the author or the Dean of Graduate Studies.

It is understood that copying or publication of this work for financial gain shall not be allowed without the author's written permission.

Permission for public performance, or limited permission for private scholarly use, of any multimedia materials forming part of this work, may have been granted by the author. This information may be found on the separately catalogued multimedia material and in the signed Partial Copyright Licence.

While licensing SFU to permit the above uses, the author retains copyright in the thesis, project or extended essays, including the right to change the work for subsequent purposes, including editing and publishing the work in whole or in part, and licensing other parties, as the author may desire.

The original Partial Copyright Licence attesting to these terms, and signed by this author, may be found in the original bound copy of this work, retained in the Simon Fraser University Archive.

Simon Fraser University Library
Burnaby, BC, Canada

Revised: Summer 2007

Abstract

Haemophilus influenzae is a Gram-negative, non-motile bacterium found in the respiratory tract of higher organisms which is naturally competent; that is, it naturally has the ability to internalise exogenous DNA. The DNA uptake machinery spans two membranes and has been shown to require an asymmetric nine basepair uptake signaling sequence to initiate DNA uptake, but the mechanism is still poorly understood. This thesis presents work toward single molecule DNA uptake experiments involving optical tweezers, including optical tweezer construction and characterization, DNA force-extension relations, plasmid design for single molecule uptake experiments, and efforts to immobilise *H. influenzae* cells to surfaces of polystyrene beads.

Acknowledgments

I would like to thank a number of people who have helped me along the way, both in the lab and out.

First, the Redfield lab at UBC for letting me learn molecular biology from them over a four month period. In particular Andrew Cameron, Milica Volar, and Lindsay Wilson, for never getting tired of my near-incessant questions on the hows and whys of running gels and enzymatic reactions, and Rosie Redfield for her endless enthusiasm and help throughout my stay (and since!).

Second, everyone from the Forde lab here at SFU. Starting a new lab can be a challenge, but the peers you have can make it much easier. This has certainly been the case for me, with good advice and suggestions from everyone. In particular I have to thank Marieke Berga for her continued help in the wet lab upon my return to SFU, and Yi Deng for instrumentation wizardry and logic puzzles in the office. I also have to thank my supervisor, Nancy, for giving me the chance to wander as far away from physics as I liked.

Finally, to everyone outside of the lab. Chad Warford for coffee and hockey, the Organic Deli for delicious lunches, Susan Penney and my family in Newfoundland for everything and then some. And Quidi the cat, for being a cat.

Contents

Approval ii

Abstract iii

Acknowledgments iv

Contents v

List of Figures vii

1 *Biological physics, in singulo* **1**
- 1.1 Measuring molecules, one by one . . . 1
- 1.2 Thesis organisation . . . 2

2 *Optical traps: theory and instrumentation* **4**
- 2.1 Principles of optical trapping . . . 4
  - 2.1.1 Ray optics . . . 5
  - 2.1.2 Scattering . . . 6
  - 2.1.3 Harmonic potentials . . . 7
- 2.2 The optical trapping instrument . . . 8
  - 2.2.1 Laser and optics . . . 8
  - 2.2.2 Trapping chambers & micropipettes . . . 9
  - 2.2.3 The flow system . . . 11
  - 2.2.4 Instrument control & bead tracking . . . 13
- 2.3 Trap calibration . . . 13

2.3.1 Retroreflection to find the trap 13
2.3.2 Converting pixels to microns 14
2.3.3 From trapped bead displacements to forces 16

3 *DNA elasticity* **23**
3.1 Elasticity theory: wormlike chains 23
3.2 Stretching DNA 27
3.2.1 Labeling DNA for single-molecule measurements 27
3.2.2 Force-extension curves 30
3.3 Sub-elastic chains 32

4 *Haemophilus influenzae and DNA uptake* **34**
4.1 *Haemophilus influenzae* 34
4.1.1 DNA uptake machinery & the Uptake Signaling Sequence 35
4.2 The uptake machinery as a molecular motor: measurable physical quantities 38
4.2.1 Linear uptake measurements 38
4.2.2 Testing uptake directionality 40

5 *Toward single-molecule DNA uptake* **43**
5.1 pPIU1: A new plasmid for DNA uptake measurements 43
5.1.1 Digestions, extractions, ligations 44
5.1.2 Transformations, harvests 45
5.1.3 pPIU1 plasmid map 48
5.2 Cell immobilisation 49
5.2.1 Non-specific interactions 49
5.2.2 Mucin 50
5.2.3 Antibodies 50
5.2.4 Analysis & further possibilities 54

6 *Conclusions* **55**

Bibliography **56**

List of Figures

2.1 Examples of ray diagrams for two different incoming beams giving rise to a gradient force on a refractive bead (index of refraction higher than the surroundings) for two illustrative rays. **a** shows a collimated beam with a linear intensity gradient and the subsequent refraction. As the right-most ray contains more photons, the change in momentum is larger for this ray than for the left-most ray, leading to a net force on the bead which points towards the high intensity region to the right. In **b**, the intensity profile is Gaussian, and the rays are now focused. In this case the refraction of the rays is symmetric, but the net change in light momentum is "downstream." In this case, the force points back towards the focal point, or region of highest intensity. Not shown in either diagram is the scattering force, which applies a force along the optic axis. Adapted from [7]. 6

2.2 Schematic of the optical tweezers instrument, where solid lines denote the laser beam and dashed lines the imaging light. See text for details. 9

2.3 Flow chamber design. The brown tubing facilitates the insertion of micropipettes in the trapping plane, while the melted Nescofilm gives a leak-proof seal for long-term reusability. 10

2.4 **a** A schematic of the pipette puller. Immobilised at the top, the glass capillary is fed through a coil of platinum wire and held under tension by a mass on the bottom. As current through the wire is increased, the local temperature is quickly raised. As the glass capillary begins to melt, the tension elongates and "pulls" a tip of the appropriate size. **b** A pipette in the chamber with a 2.1μm bead held on the tip via suction, ready for experimentation. 11

2.5 Flow system schematics. Solenoid valves are used to control the pressure applied to three $1\,mL$ syringes filled with buffers of interest, which can be individually selected for flow into the trapping chamber. A pressure transducer monitors the pressure in the system, while a manual valve selector can be used to manually inject fluid. 12

2.6 An example of the bead detection software, 'IMAQ Find Circular Edge', at work. The algorithm looks for drops in intensity along straight line profiles from specified inner and outer search radii. The position of the edge for each profile is then used to fit a circle, and the centre coordinates (x,y) and the radius are output in pixels. The inner and outer circles represent inner and outer search radii, lines are intensity profiles, with dots shown as the determined edges. The middle circle is the fit to the data. 14

2.7 Retroreflection of the laser beam is used to find the trap position when initially setting up the instrument. The laser is partially reflected by a pellicle beamsplitter, P, and retroreflected to the camera. With excellent alignment, a star-shaped pattern (from the retroreflector) is seen on the camera, with the centre giving the position of the trap in the field of view. 15

2.8 Orthogonal line profiles of a $3.17\,\mu m$ diameter bead, shown on the left. The offset is simply for clarity. Minima in intensity correspond to the dark ring surrounding the bead, and their separation gives a rough estimate of the pixel to micron ratio. 16

2.9 Position of a bead as a function of known pipette position. Horizontal motion is shown in dark grey, while vertical motion is shown in light grey (and is negative due to the (0,0) coordinate being in the top left of an image). The average of the absolute value of the slopes is measured to be $22.4 \pm 0.2\,px/\mu m$. 17

2.10 Determination of the flow velocity from a bead streak. 18

2.11 Force as a function of bead offset from the trap centre as determined by applying drag forces with fluid flow. The slope of the line gives the trap stiffness, determined here to be $k = 202.7 \pm 0.4\,pN/\mu m$. 20

2.12 Power spectrum of the noise in an optical trap. The data is fit to Equation 2.10, which gives a trap stiffness $k = 198 \pm 9\,pN/\mu m$, in good agreement with the flow measurements above. 21

3.1 Schematic of the Freely Jointed Chain model. Identical subunits of length *b* are connected by perfectly flexible hinges, allowing any angle θ between subsequent subunits. To elongate the chain, a force F is applied along the **z** axis. Adapted from [13]. 24

3.2 Schematic of the Wormlike Chain model. The conformation is described by $\mathbf{r}(s)$, where s is the position along the relaxed-state contour, with tangent vectors $\mathbf{t}(s)$. Adapted from [13]. 25

3.3 A restriction digest map of the cutting sites used in this thesis for pPIA2-6. The amp resistance gene is highlighted. 28

3.4 The sticky overhangs generated on the ends of a $12\,kb$ piece of pPIA2-6 DNA after a double digest with *EagI* and *EcoRI*. As *EagI* leaves only unpaired Cs and Gs, while *EcoRI* has unpaired As and Ts, differential labeling using bio-dCTPs and dig-dUTPs (which will bind in place of a dTTP) along with dGTP and dATP, is a single straightforward reaction. 29

3.5 Schematic of the force-extension experiment. A DNA molecule tethered between two beads is pulled taut and relaxed by the motion of the micropipette bead via computer or manual control. Experimental variables measured in this process are the bead centre-to-bead centre distance, and the offset of the trapped bead from the trap centre. The optical trap stiffness is determined prior to tethering the DNA. An off-axis DNA tether is shown as a dashed line. 30

3.6 DNA force-extension data and the associated fit to low ($F < 5\,pN$) force by the standard WLC (Equation 3.9). Good agreement between theory and experiment is evident, with some deviation from the data at intermediate forces ($F \approx 0.1\,pN$) as expected. The fit yields a persistence length $L_p = 52.0\,nm$ and an extension offset $z_0 = 2.22\,\mu m$. **Inset**–high force data shows the standard WLC model is incapable of capturing the elasticity above $\sim 5\,pN$ with these fit parameters. 32

3.7 High force ($5\,pN < F < 30\,pN$), yielding a persistence length $L_p = 52.7 \pm 0.5\,nm$ and a stretch modulus $K_0 = 1656 \pm 3pN$. This value is larger than previously reported [16], but the buffer conditions are slightly different than used in previous studies. The standard WLC fit is shown as a dashed line, and completely misses the high-force data. 33

4.1 Similarities between **a** the type IV pilus and **b** the uptake mechanism in *N. gonnorhoeae*. In type IV pili, the pilus crosses both membranes, goes through the secretin PilQ which interacts with the pilot protein PilP. In the case of the competence machinery, a DNA recognition protein (DR, yet to be discovered) lies at the tip of a secretin to bind DNA with the appropriate sequence. A periplasmic protein ComE helps deliver the DNA to ComA, a cytoplasmic membrane protein, through which the DNA enters the cytoplasm. Used with permission from D. Dubnau, from [23]. 37

4.2 Experimental geometry for linear uptake measurements, allowing measurement of force-velocity curves, stall forces, and the energy source of the motor. With the cell immobilised to the surface of a bead held in the micropipette, a linear strand of DNA containing a USS near the free end is presented to the cell for binding and subsequent uptake. Upon binding and the initiation of uptake, tracking the position of the optically trapped bead relative to cell will give information on the uptake process. 39

4.3 Experimental geometry for a proposed "three-bead assay", useful for determining linear vs bi-directional uptake. With the cell immobilised to the surface of a bead held in the micropipette, both ends of a linear strand of DNA containing a USS in the centre of the sequence are bound to distinguishable beads (for identifying orientation). Upon binding and the initiation of uptake, tracking the positions of both beads relative to cell will give information of the uptake process. 41

5.1 Unique restriction digest map for pGEM7Zf(+). A $200\,bp$ sequence including a USS inserted at the *SmaI* site creates pUSS1. From [35]. 45

5.2 Colonies of *E. coli* cells after a successful transformation of pPIU1. 46

5.3 Agarose gel (0.7%) showing the digestion of pPIU1 components and their sources. Lane 1 contains uncut pUSS1, while lane 2 contains digested (with *BamHI*, *SacI*, and *ScaI*) pUSS1. Lanes 5 and 6 contain a 1 kb ladder (Fermentas) and $\lambda/HindIII$ fragments, respectively. In lane 7 is uncut pPIU1, with its triple digest in lane 8. Lane 10 contains uncut pPIA2-6, with its double digest in lane 9. The main result is shown by the guides to the eye: pPIU1 is a combination of a section of pUSS1 (containing the USS, shown digested in lane 2) that is 3 kb in length, and a section of pPIA2-6 that is 11 kb in length. Lanes 3 and 4 contain an undesired, shorter ligation and transformation product, which is not relevant to the creation of pPIU1. . . . 47

5.4 Restriction digest map with some of the unique restriction sites for pPIU1. The USS is located around position 11200. 48

5.5 Dot blot assays for antibody-labelled beads. Anti-P2- and anti-P5-coated beads give a signal more than an order of magnitude larger than the protein-G-coated beads, signifying that anti-P2 and -P5 are in fact present on the bead surfaces. Carboxy-terminated beads show no sign of antibody, as expected. 52

5.6 Dot blot experiments showing the binding of anti-P2 and anti-P5 to the surface of competent *H. influenzae* cells. The control experiment involving no primary antibodies below shows that the signal is indeed obtained only in the presence of anti-P2 or anti-P5 sera. 53

Chapter 1

Biological physics, in singulo

1.1 Measuring molecules, one by one

A bulk system is comprised of many copies of microscopic elements, be they atoms in a crystal or proteins in a fluid environment. When taking a measurement of a bulk sample, the signal is invariably a sum of the contributions from the many different elements, each of which may be giving rise to slightly different signals. The measured signal will therefore be both a time and ensemble average over the microscopic elements. For some samples (e.g. large single crystalline materials) the bulk signal is a good representation of the microscopic dynamics, but for others, particularly chemical systems which can undergo reactions, it may not be.

A chemical system is comprised of discrete molecules undergoing stochastic, random motions, leading to reactions which occur in a random fashion. In biological systems, many enzymes have complex reaction mechanisms which are carried out over multiple steps, some of which may be reversible, may involve mechanical changes, and can proceed along alternative pathways, including irreversible stalling leading to an inactive protein. Given the complexity of this kind of system, any bulk signal will be averaged over all possible pathways, and may not be a reflection of the real underlying dynamics. Furthermore, *time* coherence of the system is also an issue. Any initial coherence in the system will quickly disappear due to the random nature of thermal fluctuations and the difference in trajectories each separate particle can take. A bulk measurement on a chemical system is then little more than "incoherent sums of the uncorrelated contributions of each molecule in the sample and can only provide the dynamics of the mean of the population but not an accurate picture of the dynamics of the individual molecules" [1].

To circumvent these averaging issues, techniques to measure the response of individual molecules have been developed – what Carlos Bustamante has termed *in singulo* experimentation [1]. This thesis will focus on optical tweezers, where a tightly focused laser beam interacting with a micron-diameter sphere acts as a handle to the world of single molecules. Optical tweezers (and other instruments like the atomic force microscope and fluorescence spectroscopy) have made it possible to measure nanometre (and smaller) motions and in the case of tweezers, forces in the picoNewton range, which is the physiologically relevant range for studying single biological molecules. With these instruments, the trajectories of a single molecule can be followed in real time, allowing direct measurement of intermediates in a reaction and alternative reaction pathways, and even the coupling of mechanical motion and forces to the underlying chemistry of an enzyme.

The ability to measure forces also presents a new direction to investigate biochemical systems. By watching the coupled mechanochemical cycle of an enzyme, the efficiency (work output to energy input) of a chemical reaction can be measured, as can the force required to stall an enzyme [2]. Similar measurements of the work required to unfold a protein or nucleic acid yields information about the free energy of the native vs unfolded states [3], intermediates in folding [4] and from a physics standpoint, fluctuations in the molecular parameters can be used as tests for fluctuation theories from statistical mechanics [5].

This thesis presents work towards measuring the uptake of DNA by the bacteria *H. influenzae* at the single molecule level using optical tweezers. This approach can address a number of unique questions inaccessible to a bulk assay, which shall be described later.

1.2 Thesis organisation

Chapter 2 of this thesis explains the theory of optical trapping and details building a single-beam optical tweezers instrument, capable of *in singulo* experiments.

The application of optical tweezers to a biological molecule is explained in Chapter 3, where double-stranded DNA stretching experiments are presented and the force-extension curves analysed in light of a polymer model.

Chapter 4 introduces the bacterium *Haemophilus influenzae* and the DNA uptake capabilities that the bacteria has. Comparisons are drawn between the *H. influenzae* machinery and other DNA uptake and translocation complexes, and single molecule experiments are proposed to test hypotheses relating to the polarity of DNA uptake.

Work carried out towards realising these single molecule assays is presented in Chapter 5, including the preparation of a new plasmid of DNA, and a variety of cell immobilisation strategies. Discussion of the results ends the chapter.

Chapter 6 concludes with a summary of the thesis.

Chapter 2

Optical traps: theory and instrumentation

What happens if a $1W$ beam is focused on a $d = 1\mu m$ bead? If you assume, as Arthur Ashkin did, that the bead acts as a perfect mirror, by conservation of momentum it is calculated that the force on the bead is on the order of 10 nanoNewtons when reflecting the beam [6]. This is an extremely small force, but for tiny masses associated with small beads, the acceleration of the bead is then $a = F/m \approx 10^5 g$, where g is the acceleration due to gravity. This order of magnitude calculation carried out by Ashkin in 1969 showed that it should be possible to levitate small objects in the focus of a laser beam, and he went about testing this hypothesis experimentally. What he found was that small latex spheres were indeed pushed by a focused beam, but that they were also drawn to the centre of the focus, would diffuse away if the laser was turned off, and would get drawn toward the centre again when turned back on. Significant advances in instrumentation and development of optical tweezers has occurred since those original experiments, but the basic physics underlying modern traps remains the same, based on the interaction of a focused laser beam with small dielectric particles. This chapter explains the principles of optical trapping and the design and construction of a single beam optical tweezer instrument.

2.1 Principles of optical trapping

A number of excellent references (including the original papers by Ashkin) exist, but a recent review article covers modern experimental and theoretical details of optical trapping quite well [7]. The arguments presented below follow this source.

2.1.1 Ray optics

The most straightforward treatment of optical trapping occurs when in the so-called Mie regime, where the trapped particle has a radius much larger than the wavelength of light ($r \gg \lambda$). In this regime, a simple ray optics approach is valid, and the cause of trapping is readily determined. Figure 2.1 gives examples of the forces on a bead in two separate beams, the first being a linear gradient, collimated beam, and the second is a Gaussian beam focused upstream from a bead. When the index of refraction of the beads is greater than the surrounding medium (a condition satisfied when water is the medium, $n = 1.33$, and the beads are made of polystyrene, $n = 1.57$), refraction of rays of light occurs at the interface between bead and water according to Snell's law, resulting in each off-axis ray incident on the bead changing direction after entering and exiting the bead. As light carries momentum and momentum is conserved, the change in momentum of the reflected light must be balanced by a change in momentum in the bead. It follows from Newton's second law that a force arises: $\mathbf{F} = d\mathbf{p}/dt$.

In Figure 2.1, part **a** shows the forces which arise when a collimated beam with linear intensity gradient impinges on a bead. While the refraction angles are symmetric with respect to the bead centre, there are more photons in the right-most ray, resulting in a net change in momentum of the light to the left (and up), and hence a force on the bead to the right (and down) – towards the highest intensity region of the beam. In this scenario, the bead gets trapped in two dimensions, however there is no mechanism for stable three dimensional trapping with this beam.

Case **b** of Figure 2.1 demonstrates that *axial* rays are required for creating a large on-axis intensity gradient that allows stable three-dimensional trapping. A high numerical aperture (NA) microscope objective (where the larger the numerical aperture, the more tightly focused the rays are) that has been overfilled such that there is still significant intensity in the most axial rays is used in the laboratory to achieve a stable trap.

The forces described to now are called *gradient* forces, as they arise due to gradients in the light intensity. Not shown in Figure 2.1 is the scattering force, which arises, not surprisingly, from backscattered and absorbed light. In this case the change in light momentum gives rise to a force on the bead that points along the optic axis, pushing the bead like a "photon fire hose" [7]. In a stable three-dimensional trap, the scattering force and gradient

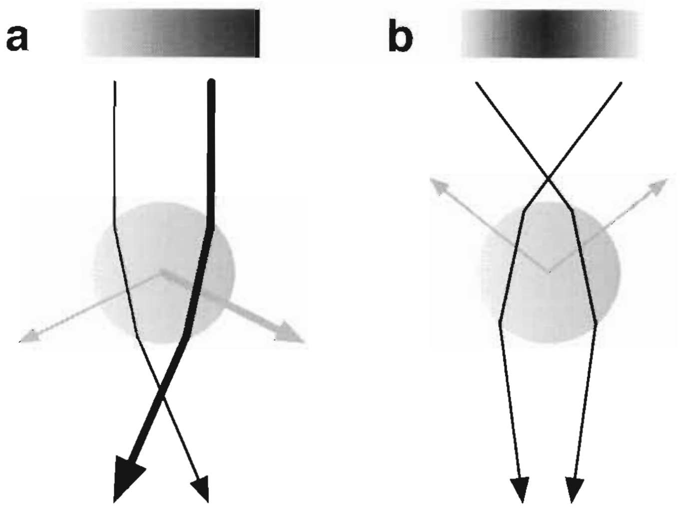

Figure 2.1: Examples of ray diagrams for two different incoming beams giving rise to a gradient force on a refractive bead (index of refraction higher than the surroundings) for two illustrative rays. **a** shows a collimated beam with a linear intensity gradient and the subsequent refraction. As the right-most ray contains more photons, the change in momentum is larger for this ray than for the left-most ray, leading to a net force on the bead which points towards the high intensity region to the right. In **b**, the intensity profile is Gaussian, and the rays are now focused. In this case the refraction of the rays is symmetric, but the net change in light momentum is "downstream." In this case, the force points back towards the focal point, or region of highest intensity. Not shown in either diagram is the scattering force, which applies a force along the optic axis. Adapted from [7].

force must balance, again made possible when a microscope objective is used to create a highly converging beam.

2.1.2 Scattering

In the so-called Rayleigh regime, objects have radii much smaller than the wavelength of light ($r \ll \lambda$). In this regime we may consider the trapped object as a point dipole, and the scattering and gradient forces are well known [7]. The scattering force arises due to absorption and subsequent re-emission of light, which for a spherical body of radius r is given by

$$F_s = \frac{I_0 \sigma n_m}{c}, \tag{2.1}$$

where I_0 is the beam intensity, c is the speed of light, n_m is the index of refraction of the surrounding medium, and σ is the scattering cross section, given by

$$\sigma = \frac{128\pi^5 r^6}{3\lambda^4}\left(\frac{m^2-1}{m^2+2}\right)^2,$$

where m is the ratio of the particle index to medium index, n_p/n_m. The gradient force, which still must overcome the scattering force to stably hold the particle in three dimensions, is due to the interaction of the dipole with the gradient of light intensity,

$$F_g = \frac{2\pi\alpha}{cn_m^2}\nabla I_0, \tag{2.2}$$

where the polarisability of the dipole is given by

$$\alpha = n_m^2 r^3 \left(\frac{m^2-1}{m^2+2}\right).$$

Again we see that the gradient force is directed towards the region of highest light intensity gradient (given by ∇I_0) for $n_p > n_m$, in agreement with the ray diagram approach above.

Unfortunately, the ideal size of particles used in experiments involving biological molecules falls into a regime between the Rayleigh and Mie limits. Neither of the above models applies readily to particles where $r \approx \lambda$, and full electromagnetic theory calculations are both cumbersome and do not entirely agree with experimentally measured values [8]. There are also practical limitations on bead size as well. If one wishes to use an optical microscope in conjunction with the trapping laser, the diffraction limit imposes a minimum size constraint on bead imaging. Conversely, larger beads are difficult to manipulate, as the field of view in the optical microscope is limited. Fortunately, it isn't necessary to predict the trap stiffness as it can be experimentally determined prior to experimentation involving force measurement.

2.1.3 Harmonic potentials

To a good approximation the optical trap can be modelled as a harmonic potential as a result of the focussed Gaussian intensity profile (as in Figure 2.1 b), where a bead held in the trap feels a force due to the potential $U = \frac{1}{2}kx^2$. For large values of x the potential deviates from this parabolic form, but for small values of displacement the bead feels a force of

$$F = -\nabla U = -kx, \tag{2.3}$$

where k is the optical trap stiffness. As the bead is displaced from the trap centre ($x = 0$), a force proportional to this displacement acts on the bead.

2.2 The optical trapping instrument

From the preceding section, it is clear that we need a highly focused laser beam to trap, but to accurately measure picoNewton forces and nanometre displacements requires much more. The following sections give details about the design and construction of a single-beam optical tweezers instrument based on a previous flow control/video microscope optical trap [9].

2.2.1 Laser and optics

A schematic of the laser and optics for trapping and imaging is detailed in Figure 2.2. This instrument is built on a vibration-isolating optical table. The trapping beam comes from a $\lambda = 835nm$, $200mW$ beam single-mode diode laser (beam diameter 8mm, assembled by Melles Griot with a diode from JDS Uniphase, FG5431-G1-830-10-G1-.2), whose wavelength was chosen for its minimal absorption in water and photo-damage to living cells [10]. The beam is sent through a fast mechanical shutter S (Melles Griot, 04 UTS 201), through a Faraday isolator FI (Optics for Research, IO-10-834-LP) to prevent backscattered light from reaching the laser cavity, reflected by a polarising beamsplitter cube PBS (Melles Griot, 03 PBS 067) and sent to a plan apochromatic, infinity corrected, 60×, water immersion, NA=1.2 objective lens (Olympus, UPLSAPO60XW). This objective is the focusing lens and creates an optical trap in the trapping chamber described in the following section. A second identical objective recollimates the beam, which is then reflected by a second polarising beamsplitter and sent to a 2D position-sensitive duo-lateral silicon photodiode (DL10, OSI Optoelectronics), which is itself connected to a fast PC. At the DL10, the beam power is approximately 50% that of the power entering the first objective ($160mW$), giving the objectives each a transmission of 70% at $\lambda = 835nm$.

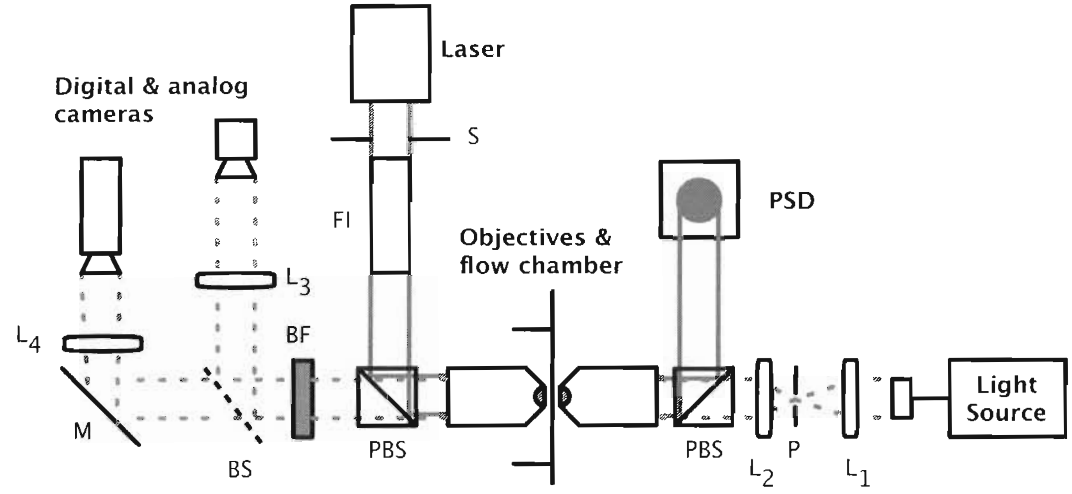

Figure 2.2: Schematic of the optical tweezers instrument, where solid lines denote the laser beam and dashed lines the imaging light. See text for details.

The imaging microscope begins with a Fiber-Lite 180 (Dolan-Jenner Industries) high-intensity white light source, focused to a manual iris diaphragm *P* (Thorlabs, ID12) by lens L_1 ($f = 4cm$). L_2 ($f = 5cm$), placed a focal length away from the pinhole, sends collimated light to the objectives. After exiting the objectives, the light is sent through a blue filter (BG38, Melles Griot) to eliminate laser light and a 50:50 beamsplitter to a digital camera (Flea, Pt. Grey), imaged by L_3 ($f = 400mm$), and an analog camera with a wide field of view (L_4 has a focal length $f = 150mm$). The analog camera is connected to a black and white CCTV, while the Flea is connected to the PC. The Flea collects images at a resolution of 640×480 pixels at $60Hz$.

2.2.2 Trapping chambers & micropipettes

Homemade flow chambers are made for trapping experiments, shown in Figure 2.3. Sandwiched between two No. 1 microscope coverglasses (thickness $0.17mm$) are two layers of Nescofilm (Karlan, N-1040), containing a channel cut manually by razor blade. Between these is a $3mm$ length of "brown tubing" (OD $164\mu m$, ID $100\mu m$, Microfil34G, World Precision) which allows insertion of a micropipette. The topmost coverslip has input and

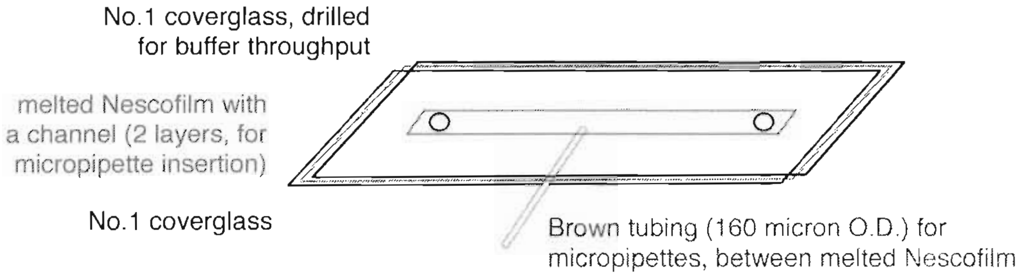

Figure 2.3: Flow chamber design. The brown tubing facilitates the insertion of micropipettes in the trapping plane, while the melted Nescofilm gives a leak-proof seal for long-term reusability.

output holes drilled at either end of the Nescofilm trough by a diamond-tipped bit approximately $2\,mm$ in diameter prior to chamber construction. The chamber is then sealed at $393\,K$ for $\sim$10 minutes, or until a sufficient seal has been created by the melted Nescofilm.

When properly cared for (left clean and dry when not in use to prevent the growth of bacteria), these chambers can last for months.

Micropipettes are used as another handle for beads in the chambers, and are homemade as well (see Figure 2.4). A glass capillary (OD $0.08\,mm$, ID $0.04\,mm$, Garner Glass Company, KG-33) immobilised at the top of a pipette puller is fed through the centre of a coil ($d = 1.5\,mm$) of platinum wire connected to a homemade power supply. It is clamped at its bottom end, and by ramping up the current through the platinum wire, temperatures sufficiently high to melt the glass are reached at the centre of the coil. As the glass begins to melt, the tension pulls the capillary such that it tapers and is eventually pulled free to form a solo pipette.

To couple the extremely small capillary to a syringe for manual suction control, the capillary is inserted in polyethylene tubing (PE10, Intramedic) and melted by a heat gun. To constrain the melting of the PE10 tubing to the region around the glass capillary, narrow diameter heat shrink tubing encases this region (otherwise an airtight seal is extremely difficult to create). The pipette is then inserted into the brown tubing and is ready to hold beads via suction in the middle of the chamber.

To move the pipette relative to the fixed optical trap position, the chamber with enclosed

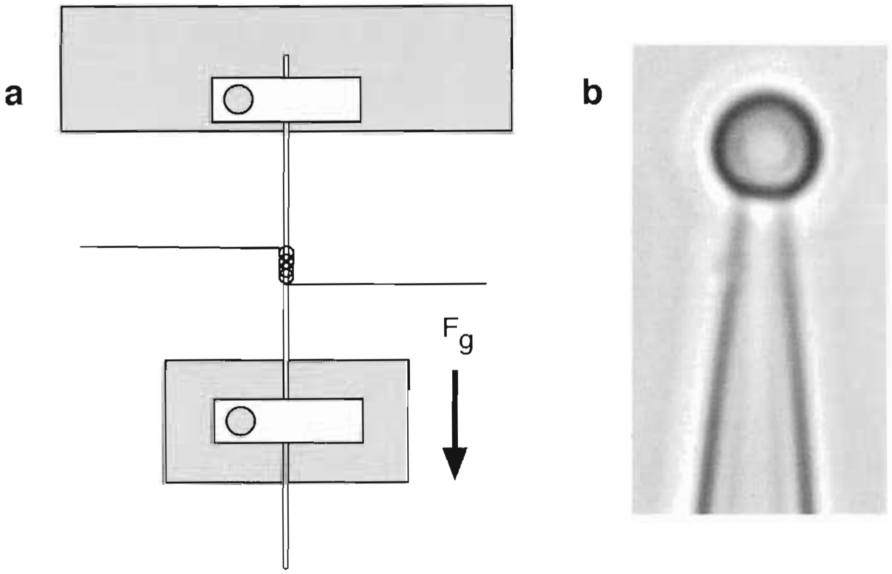

Figure 2.4: **a** A schematic of the pipette puller. Immobilised at the top, the glass capillary is fed through a coil of platinum wire and held under tension by a mass on the bottom. As current through the wire is increased, the local temperature is quickly raised. As the glass capillary begins to melt, the tension elongates and "pulls" a tip of the appropriate size. **b** A pipette in the chamber with a $2.1\mu m$ bead held on the tip via suction, ready for experimentation.

pipette is mounted on a high resolution 2-axis piezoelectric stage (Nano H50, Mad City Labs). This stage has a range of $50\mu m$ in both x and y, a resolution of $0.3nm$, and is controllable by PC. This allows exquisite control of the relative position of the micropipette to the trap centre, and can also be used to feed back to create a force- or extension-clamp, that is, a constant force or constant molecular extension over time.

2.2.3 The flow system

The instrument is also equipped with a flow system for buffer exchange and flow control, shown in Figure 2.5. Three solenoid valves (Clippard Minimatics, EV-2-24) are connected to pressure, atmosphere, and mild vacuum line sources from the departmental liquid nitro-

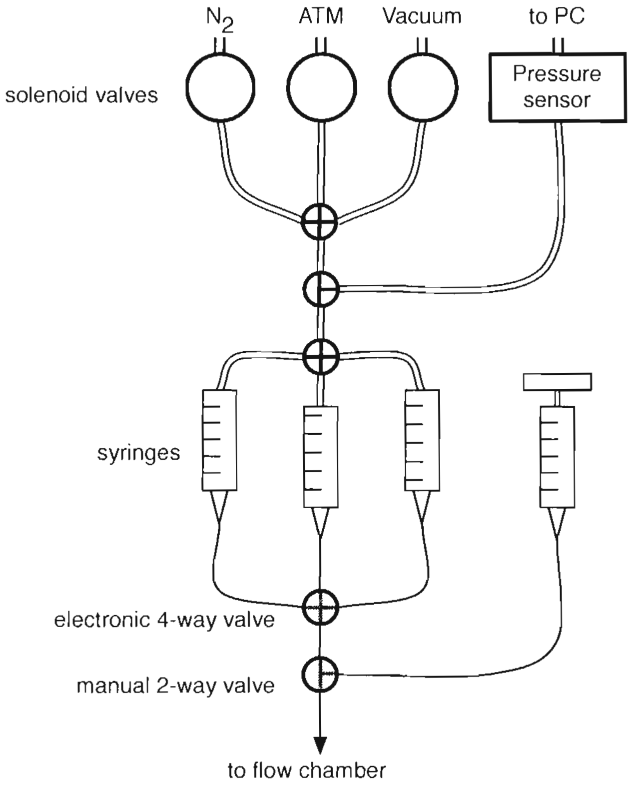

Figure 2.5: Flow system schematics. Solenoid valves are used to control the pressure applied to three $1\,mL$ syringes filled with buffers of interest, which can be individually selected for flow into the trapping chamber. A pressure transducer monitors the pressure in the system, while a manual valve selector can be used to manually inject fluid.

gen boil off, the ambient environment, and a water aspirator respectively, and pressure in the system (to a maximum of $\pm 125\,kPA$ relative to the atmospheric pressure) is measured by a pressure transducer (Motorola, MPX2200AP). These are connected by polyethylene tubing (Intramedics, PE10-100) to $1\,mL$ syringes (BD Scientific), which contain solutions of beads, buffers, and molecules of interest. By applying pressure to the syringes, liquid flows through an electronic valve selector (MVP-4, Hamilton) with HPLC fittings (Upchurch Scientific). Downstream, a manual valve selector (HV3-2, Hamilton) also offers manual injection.

The solenoid valves are all computer controlled, allowing either continuous or pulsed control for macroscopic or fine adjustment of the pressure.

2.2.4 Instrument control & bead tracking

For instrument control, custom software has been written in National Instruments LabVIEW 8, with an NI BNC-2090 DAQ board and 6052E DAQ card for interfacing between the PC and the DL10 photodiode, the high resolution piezoelectric stage, the flow system, the mechanical shutter release, and the pressure sensor. NI IMAQ 2.1 is used for image acquisition, and NI Vision 7.1 for image analysis.

For bead tracking, the 'IMAQ Find Circular Edge' algorithm is used. As shown in Figure 2.6, once given a circular search area in terms of inner and outer radius (circles), line profiles (lines) are taken from the outer to inner circular search region at specified angular steps. After determining edge locations from drops in intensity along the line profiles (points), the algorithm fits a circle to the data and outputs the bead radius and centre coordinates in pixels. Sub-pixel (corresponding to $\approx 5\,nm$) resolution is attainable with sufficiently many line profiles (small angular stepsizes) and bright, well aligned illumination.

2.3 Trap calibration

To use the optical trap as a high-resolution position- and force-detecting instrument, two constants must be experimentally determined: the pixels to microns conversion factor of the images, and the optical trap stiffness. But first we must find the the trap.

2.3.1 Retroreflection to find the trap

When initially constructing an optical trapping instrument, using a pair of microscope objectives in lieu of an inverted microscope means the imaging system is not pre-aligned. As such, it can be difficult to find the position of the trap. One way to find the trap involves the use of a pellicle beam splitter (Thorlabs, BP108) positioned before the first objective, which sends 8% of the laser to a retroreflector (Thorlabs, PS971). The retroreflected beam is reflected by the pellicle again, letting a small amount of light reach the camera as shown in Figure 2.7. With excellent alignment, a star-shaped pattern (from the retroreflector) is seen on the camera, with the centre giving the position of the trap in the field of view.

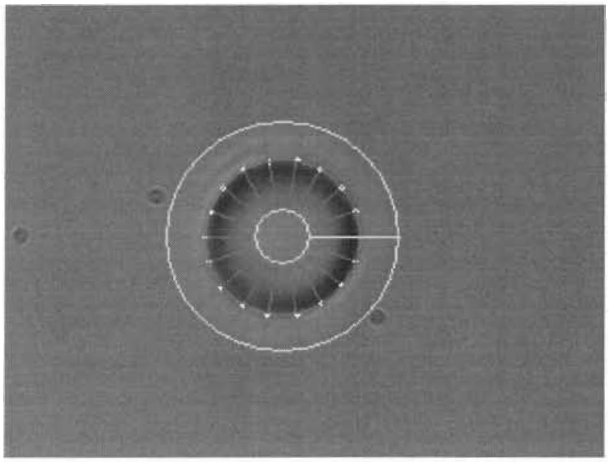

Figure 2.6: An example of the bead detection software, 'IMAQ Find Circular Edge', at work. The algorithm looks for drops in intensity along straight line profiles from specified inner and outer search radii. The position of the edge for each profile is then used to fit a circle, and the centre coordinates (x,y) and the radius are output in pixels. The inner and outer circles represent inner and outer search radii, lines are intensity profiles, with dots shown as the determined edges. The middle circle is the fit to the data.

2.3.2 Converting pixels to microns

The digital camera used to visualise the trapping plane captures images as eight-bit 640×480 pixel arrays which must be calibrated so that the absolute size of objects and distances in the image are known. One way to do this is to use an object of known size in the image. The most readily available objects with a well defined size are (in principle) the polystyrene beads. These beads can be purchased in sizes ranging from tens of nanometres to tens of microns, and common sizes for our instrument are two to three microns in diameter. By looking at line profiles of beads with well characterised sizes, it should be possible to determine the pixel to micron calibration factor from a trapped bead.

Bead line profiles

Figure 2.8 shows a nominally $3.17\mu m$-diameter carboxy-terminated polystyrene bead (Spherotech, Inc.) and associated intensity profiles. The image was analysed in National Instruments Vi-

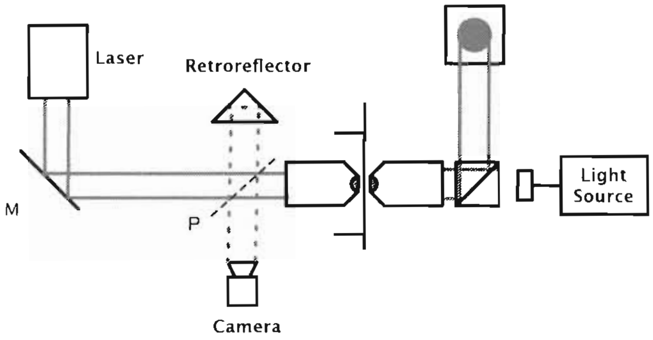

Figure 2.7: Retroreflection of the laser beam is used to find the trap position when initially setting up the instrument. The laser is partially reflected by a pellicle beamsplitter, P, and retroreflected to the camera. With excellent alignment, a star-shaped pattern (from the retroreflector) is seen on the camera, with the centre giving the position of the trap in the field of view.

sion Assistant 7.1 using the Line Profile tool, which outputs intensity along a user-specified line.

As can be seen from the image, the circumference is made up of a wide, dark ring, and it is not clear where the edge of the bead is located inside this region of low light intensity. Indeed, experiments involving a trapped bead and another bead held on the tip of a pipette have shown that beads are brought into contact only *after* overlapping the dark rings. As such, it is not possible to get a reliable value for the pixel to micron conversion from a trapped bead alone. Additionally, standard deviation in bead size is quoted at $0.05\mu m$ from the manufacturer. However, as a ballpark figure, the distance between minima of the intensity profiles between both axes averages to $68.5\,px$ ($68\,px$ along x, $69\,px$ along y, respectively), which gives $68.5/3.17 = 21.6\,px/\mu m$.

Stage displacements

A better way to determine the pixel to micron conversion is to make use of the factory-calibrated high-resolution piezoelectric stage upon which the chamber (and therefore micropipette) is mounted. As this is already calibrated, it offers an independent method of measuring distances by stepping the stage known amounts and observing displacements

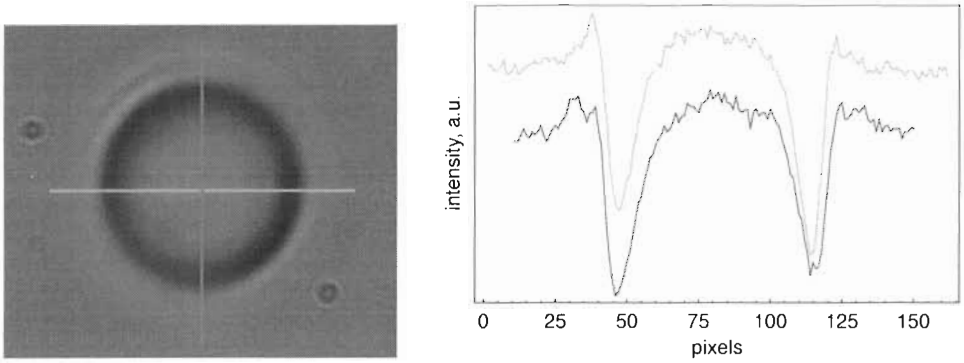

Figure 2.8: Orthogonal line profiles of a $3.17\,\mu m$ diameter bead, shown on the left. The offset is simply for clarity. Minima in intensity correspond to the dark ring surrounding the bead, and their separation gives a rough estimate of the pixel to micron ratio.

with the digital camera of a bead held by suction to a micropipette tip. While this method still uses a bead for calibration, the issue above is mitigated by the fact that only the *centre* of the bead, which can be reliably determined by the edge detection algorithm, is required for calibration.

Figure 2.9 shows a plot of the bead centre position as the stage (pipette) is moved by known amounts. The slope of the best fit gives the conversion factor from pixels to microns, as desired. Averaging over both x and y, $<\text{slope}> = 22.4 \pm 0.3\, px/\mu m$. As this method is independent of the nuances of bead imaging, this value is a better representation of the pixel to micron conversion factor, and is used for the rest of the measurements in this thesis.

2.3.3 From trapped bead displacements to forces

Now that our digital image is properly calibrated, the optical trap stiffness can be accurately determined. While there are many ways to measure this quantity (see e.g. [7]), this thesis will focus on Stokes' drag measurements and briefly discuss analysis of the power spectrum of a bead held in a trap.

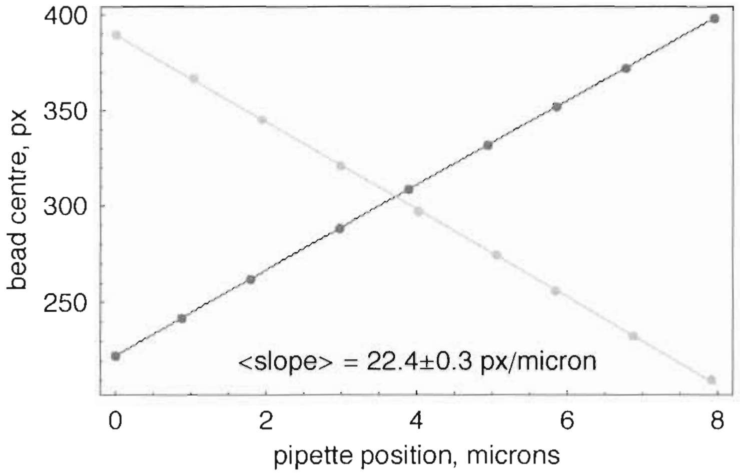

Figure 2.9: Position of a bead as a function of known pipette position. Horizontal motion is shown in dark grey, while vertical motion is shown in light grey (and is negative due to the (0,0) coordinate being in the top left of an image). The average of the absolute value of the slopes is measured to be 22.4 $\pm 0.2\, px/\mu m$.

Flow rates

With the flow system described previously, we are not only able to change the buffer conditions at the trap position, we are also able to apply forces of known amounts using flow of specified velocities. To do this, we must calibrate the pressure transducer voltage output with the actual velocity of flow in the chamber.

The field of view in our chamber is approximately $40\mu m \times 30\mu m$, so it quickly becomes impossible to measure flow rates of any 'substantial' speed in real time – the beads streak by too quickly. Instead, fast velocities are measured by looking at streaks of beads in single frames. The camera shutter is only open for a specified amount of time, and if the bead is moving sufficiently quickly it will be displaced during this small timeframe. As such, it will appear as a streak in a single image. With knowledge of the pixel to micron calibration factor and the shutter time of the image, the streak can be used to determine flow rates.

To obtain bead streaks, a bead is held in the optical trap while the pressure is raised to increase fluid velocity. At the desired pressure, the mechanical shutter blocks the laser beam and this is used as a trigger for the digital camera to begin acquiring images. As the mechanical shutter closes, the bead is caught up in the laminar flow and displaced at the same rate as the surrounding fluid. Acquiring 6 images subsequent to the closing of the laser shutter, the best streak (one that is fully contained in an image) is then chosen for measurement. An example of a bead streak is shown in Figure 2.10.

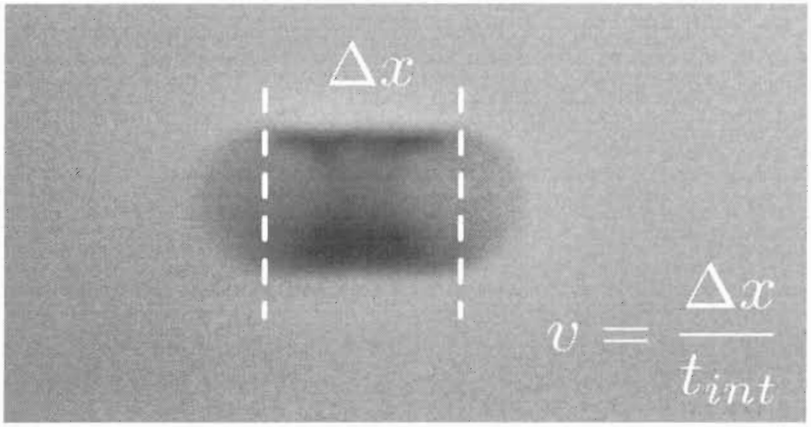

Figure 2.10: Determination of the flow velocity from a bead streak.

As the images are quite grainy, significant processing would be required for full automation of bead centre to bead centre determination. Instead, manually measuring bead centre differences has proven reliable to within $\pm 2px$, and has been used in lieu of an automated program for streak length measurements. For large pressures (high laminar flow rates), streaks are hundreds of pixels in length, so the uncertainty above is on the order of $\approx 1\%$.

The integration time for an image is set by the camera's shutter speed. The Flea camera used in our instrument outputs the integration time as a shift register in IEEE/REAL×4 format. Reading register 0×F0F0 0918 will output a 32-bit binary number, divided up as $S|EXP|FACTOR$. S is the first bit, EXP the following eight bits, and $FACTOR$ are the final 23. The following formula will calculate the actual camera integration time in units of seconds,

$$t_{int} = (-1)^S \times 1.FACTOR \times 2^{(EXP-127)}. \tag{2.4}$$

Knowing the integration time for the image being analysed, the velocity is readily determined by dividing the length of the streak (converted to metres from the now-known pixels to microns conversion factor) by the integration time. Carrying out this procedure for a sequence of voltages gives the pressure (in Volts) to velocity conversion necessary for Stokes' drag analysis. This should be calibrated each day before and during experimentation involving fluid flow.

Stokes' drag

With the ability to impose flow of known velocities in the trapping chamber, it is now possible to apply known forces to spherical objects, and measure the response via optical tracking. The hydrodynamic drag on a sphere in laminar flow ($Re = \rho v r/\eta \approx 10^{-3}$ for an $r = 1\,\mu m$ bead in a flow field of $1\,mm/s$ in water, where $\eta = 10^{-3}\,Pa \cdot s$, $\rho = 10^{6}\,g/m^{3}$) leads to a Stokes' drag force, given by

$$F = \gamma v = 6\pi\eta r v \tag{2.5}$$

where η is the viscosity of the fluid, r is the radius of the sphere, and v the velocity of the flow. As our trapping chamber is quite small, it is possible that the drag felt by the sphere will be modified by Faxen's law, which considers interactions between a sphere an an infinite surface. To fifth order, the drag coefficient now takes the form [7]

$$\gamma_{Faxen} = \frac{6\pi\eta r}{1 - \frac{9}{16}\left(\frac{r}{h}\right) + \frac{1}{8}\left(\frac{r}{h}\right)^{3} - \frac{45}{256}\left(\frac{r}{h}\right)^{4} - \frac{1}{16}\left(\frac{r}{h}\right)^{5}}. \tag{2.6}$$

where h is the separation between the bead centre and the surface. Substituting values for our bead and chamber geometry ($r \approx 1\mu m, h \approx 100\mu m$) shows that our drag coefficient is modified by less than 0.6%, so the canonical Stokes law (Equation 2.5) is used instead.

The result of applying a drag force to a trapped $2.1\,\mu m$ diameter bead is shown in Figure 2.11. Upon increasing the force on the trapped bead by increasing the flow rate, a linear relationship between force and displacement from the trap center (the bead position when $v = 0$), is observed as expected. A linear fit to the data having a functional form

$$F = -kx \tag{2.7}$$

gives a trap stiffness value of $k = 202.7 \pm 0.4 pN/\mu m$.

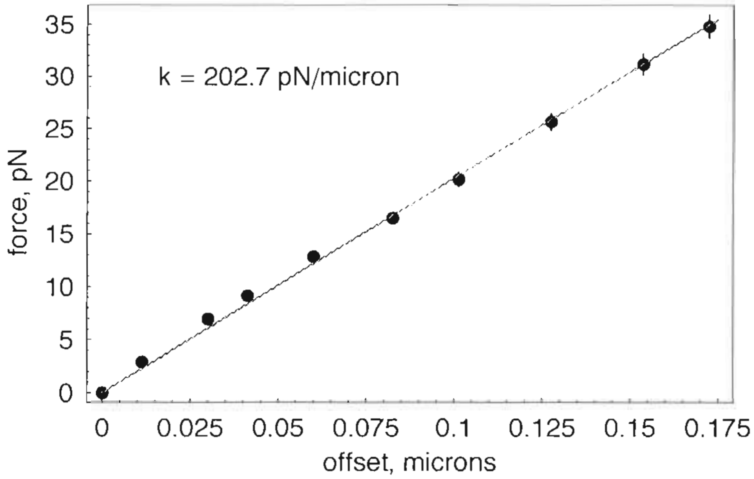

Figure 2.11: Force as a function of bead offset from the trap centre as determined by applying drag forces with fluid flow. The slope of the line gives the trap stiffness, determined here to be $k = 202.7 \pm 0.4\, pN/\mu m$.

Power spectrum of Brownian motion

Another measure of the trap stiffness analyses the position of the laser beam downstream of the trapping plane. As the bead held in the optical trap fluctuates about the trap centre due to Brownian motion, the laser too will be deflected from its normal equilibrium position, and this position fluctuation can be measured by the position-sensing photodetector.

The motion of a bead held in an optical trap subjected to Brownian motion is well described by the Langevin equation [11]:

$$m\ddot{x}(t) + \gamma\dot{x}(t) + kx(t) = \sqrt{2k_BT\gamma}F(t) \tag{2.8}$$

where m is the mass of the bead, $x(t)$ is the bead position as a function of time, γ is the drag coefficient, k the trap stiffness, k_B is Boltzmann's constant, T is temperature in Kelvin, the term on the right represents the random thermal force with $F(t)$ a Gaussian with a mean of zero and a standard deviation of 1. Because the system is overdamped, the inertial term ($m\ddot{x}(t)$) can be safely dropped, and we are left with

$$\dot{x}(t) + 2\pi f_c x(t) = \sqrt{2D}F(t) \tag{2.9}$$

where $f_c = k/2\pi\gamma$ is known as the corner frequency, and $D = k_BT/\gamma$ is the bead's diffusion constant.

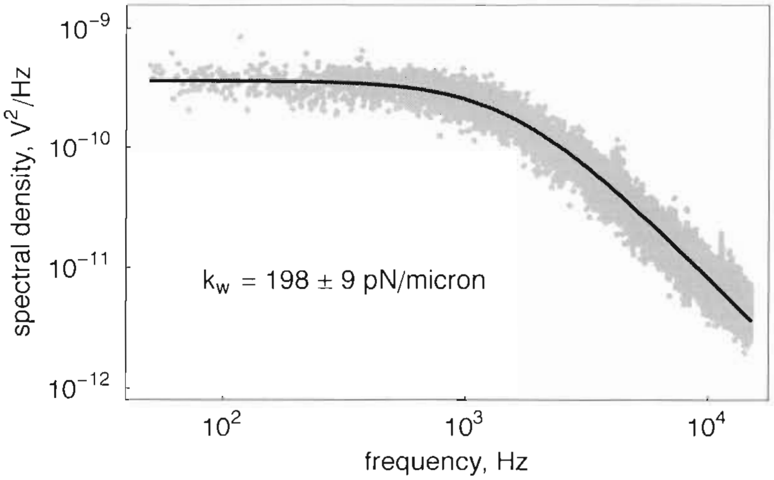

Figure 2.12: Power spectrum of the noise in an optical trap. The data is fit to Equation 2.10, which gives a trap stiffness $k = 198 \pm 9\,pN/\mu m$, in good agreement with the flow measurements above.

If we collect a significant amount of position data (multiple seconds of data at $60kHz$), we can look at the power spectrum of the position signal. This power spectrum can be approximated as a Lorentzian (see [12, 11]), given by

$$S(f) = \frac{D/2\pi^2}{f_c^2 + f^2} \tag{2.10}$$

where f is frequency. At low frequencies the power spectrum $S(f)$ is dominated by the square of f_c and is a constant, but as $f > f_c$ the spectrum decays as f^{-2}. The trap stiffness is related to the corner frequency by

$$k = 12\pi^2 f_c \eta r \tag{2.11}$$

where η is again the viscosity, and r the bead radius. Thus, a fit of the power spectrum to Equation 2.10 gives, with knowledge of the fluid medium and bead size, the optical trap stiffness. Such a plot is shown in Figure 2.12, with the associated fit giving a value of $k = 198 \pm 9\,pN/\mu m$, where the error is given by fluctuations observed in measured k values over repeated power spectra of the same bead. This value is in good agreement with the Stokes' drag method above, though it is noted that the same bead was not used for both experiments (as beads used for flow measurements are swept away with the flow).

For a given optical alignment, the trap stiffness is generally constant over a timespan of months to within $\pm 10\%$.

Chapter 3

DNA elasticity

This chapter presents analysis of the force-extension relation of double-stranded DNA (ds-DNA). Stretching an individual DNA polymer allows one to investigate elasticity properties, and information regarding the so-called persistence length, or how floppy a chain the polymer is, can be determined from the force-extension relation.

3.1 Elasticity theory: wormlike chains

This section closely follows the treatment by Storm & Nelson [13]. Physicists are first introduced to elasticity theory under the guise of spring compression and extension and Hooke's law, which relates the force required to hold a spring in a non-equilibrium extension. It is normally written

$$F = -kx, \tag{3.1}$$

where F is the reaction force of the spring, x is the spring's extension (or compression) from equilibrium, and k is the spring constant relating the two. The minus sign implies, as it did in Chapter 2 for the optical trap stiffness, that this is a *restoring* force.

However, there are very few materials that follow Hooke's law for all forces. Many exhibit nonlinear force-extension relations that require higher-order terms in x. Unlike macroscopic springs, individual polymer molecules have nonlinear elasticities – they aren't Hookean. However, many polymers are also very long (hundreds of microns in length) compared to their diameters (on the order of a nanometre), and are made of many repeat-

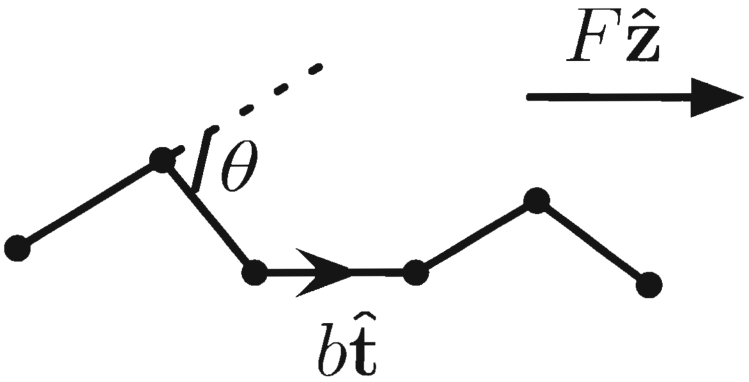

Figure 3.1: Schematic of the Freely Jointed Chain model. Identical subunits of length b are connected by perfectly flexible hinges, allowing any angle θ between subsequent subunits. To elongate the chain, a force F is applied along the **z** axis. Adapted from [13].

ing subunits. Because of this, it perhaps isn't surprising that a quantitative model of the elastic properties doesn't depend on their microscopic details. The simplest model (beyond Hooke's law) is called the Freely Jointed Chain, where subunits of length b are joined by perfectly flexible hinges, as shown in Figure 3.1.

When a force F is applied, the energy of the chain (having N repeating subunits) takes the form [13]

$$\frac{E}{k_BT} = -\sum_{i=1}^{N} \frac{Fb}{k_BT}\hat{\mathbf{t}}_i \cdot \hat{\mathbf{z}}, \tag{3.2}$$

where k_B is Boltzmann's constant, T is temperature in Kelvin, $\hat{\mathbf{t}}_i$ is the orientation vector of the ith subunit, and $\hat{\mathbf{z}}$ is the direction of the applied force. If the applied force were removed then all configurations would have the same energy and the chain would follow a random walk. To extend such a chain requires removing the *conformational entropy* from the system, and an analytic solution for the force-extension relation has been determined [14]:

$$\left\langle \frac{z}{L_0} \right\rangle = \coth\left(\frac{Fb}{k_BT}\right) - \frac{k_BT}{Fb}, \tag{3.3}$$

where L_0 is the contour length of the molecule. In the low-force limit (expanding the

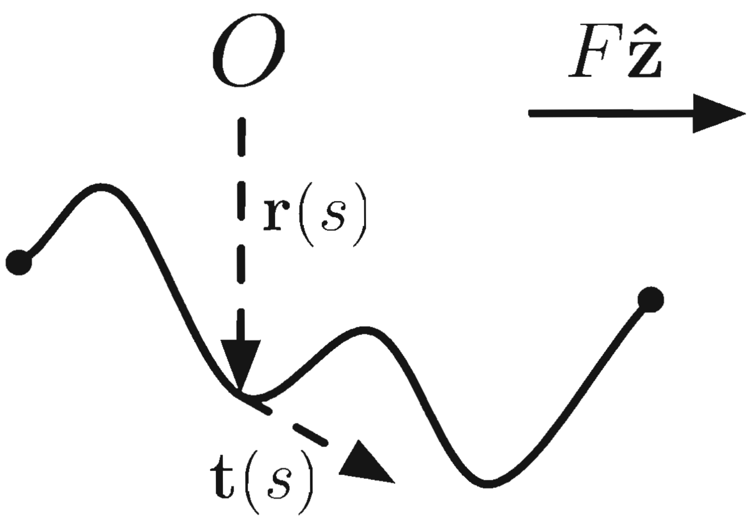

Figure 3.2: Schematic of the Wormlike Chain model. The conformation is described by $\mathbf{r}(s)$, where s is the position along the relaxed-state contour, with tangent vectors $\mathbf{t}(s)$. Adapted from [13].

hyperbolic cotangent about 0), this reduces to

$$\left\langle \frac{z}{L_0} \right\rangle \Big|_{F\to 0} \approx \frac{b}{3k_BT}F \tag{3.4}$$

which has a Hooke's law form. Furthermore, it shows that the spring constant is proportional to the temperature, as expected for an entropic "spring".

Double-stranded DNA, however, does not follow a FJC. The low force regime, where extension is linear with applied force, is a common characteristic of all polymer models [13], but at higher force this model fails to describe dsDNA (see Section 3.2.2). As such, modifications to the FJC model are needed to describe the data well. To do this, *cooperativity* within the chain must be taken into account: segments of the chain close together will, more often than not, point in nearly the same direction. Instead of being comprised of discrete segments of length b, the polymer is now treated as a continuous chain, as shown in Figure 3.2. This model is known as the Wormlike Chain (WLC).

As a continuous rod, we can now define the position $\mathbf{r}(s)$ and tangent vector $\mathbf{t}(s)$ as a function of the length along the relaxed-state contour s. A curvature vector $\mathbf{w}(s)$ can also be defined, with

$$\mathbf{t}(s) = \frac{d\mathbf{r}(s)}{ds}, \quad \mathbf{w}(s) = \frac{d\mathbf{t}(s)}{ds}.$$

For a long thin rod, the elastic energy is proportional to the square of the curvature [13], so the equivalent of Equation 3.2 for the WLC model is:

$$\frac{E}{k_BT} = \int_0^{L_0} \left[\frac{L_p}{2} |\mathbf{w}(s)|^2 - \frac{F}{k_BT} \mathbf{t}(s) \cdot \hat{\mathbf{z}} \right] ds, \tag{3.5}$$

where a new phenomenological parameter has entered the energy term, L_p, which is the persistence length of the chain, or how long a segment of the chain will have correlated tangent vectors. Indeed, the tangent-tangent correlation function for the wormlike chain at zero stretching force is given by

$$\langle \mathbf{t}(0) \cdot \mathbf{t}(s) \rangle \sim e^{-|s|/L_p}.$$

It can also be seen that, in contrast with the FJC, in the absence of applied force all conformations are no longer equally probable, due to the energy cost of bending the chain.

An analytical form of the force-extension relation for the inextensible WLC formulated above is not known; however, an interpolation formula that captures the force-extension behaviour of DNA at both low and high forces (with slight deviations at intermediate values of $F \approx 0.1\,pN$) has been numerically determined (see [15]). Reproduced here, the WLC interpolation formula is

$$F = \frac{k_BT}{L_p} \left(\frac{1}{4(1 - z/L_0)^2} - \frac{1}{4} + \frac{z}{L_0} \right). \tag{3.6}$$

At low forces ($z/L_0 \rightarrow 0$) this reduces again to Hooke's law, with the effective spring constant given by $k = 3k_BT/2L_p$, in agreement with the FJC low-force constant for $b = 2L_p$. In the high-force limit, $z \rightarrow L_0$ goes as $1/\sqrt{F}$, which will be shown to be in good agreement with the data, with slight modifications. In general, this formula is applicable for low forces ($F < 5pN$) [16].

Modifications to the WLC

As mentioned, the inextensible WLC model described above is not valid over the entire range of a force-extension curve. The low-force data is well fit by the WLC, but as forces increase not only does the DNA strand become straightened, but *enthalpy* must be accounted for as well. A number of similar approaches to incorporating an enthalpic correction to the WLC have been introduced. One such modification to the wormlike chain formula from Equation 3.6 replaces all z/L_0 terms with $z/L_0 - F/K_0$, where F is the force and K_0 is the stretch modulus of DNA, which takes into account deformations of the bond angles in the phosphate backbone of the DNA at high forces. The "extensible" WLC force-extension relation is therefore

$$F = \frac{k_B T}{L_p}\left(\frac{1}{4(1 - z/L_0 + F/K_0)^2} - \frac{1}{4} + \frac{z}{L_0} - \frac{F}{K_0}\right). \tag{3.7}$$

This formulation is known as the *extensible* WLC, and while it still has difficulties at intermediate forces ($F \approx 0.1 pN$), the high-force data are captured quite accurately. In fact, focusing only on the high-force regime and dropping the linear terms results in

$$F = \frac{k_B T}{L_p}\left(\frac{1}{4(1 - z/L_0 + F/K_0)^2}\right).$$

This can be rearranged to give

$$z = L_0\left(1 - \frac{1}{2}\sqrt{\frac{k_B T}{F L_p}} + \frac{F}{K_0}\right) \tag{3.8}$$

which is the result of Odijk [17], giving the extension as a function (nonlinearly) of force, applicable to the high-force regime.

3.2 Stretching DNA

3.2.1 Labeling DNA for single-molecule measurements

To experimentally apply the above models, we need to stretch DNA molecules in the optical tweezers instrument described in Chapter 2. The polystyrene spheres introduced in the previous chapter can be functionalised to act as handles for biophysical experiments, with modifications to the individual DNA molecules leading to strong links between beads and the DNA. The interactions used in these experiments involve streptavidin and anti-digoxigenin coated polystyrene beads (Spherotech Inc.), with biotin and digoxigenin (dig) used as complements in the modified DNA.

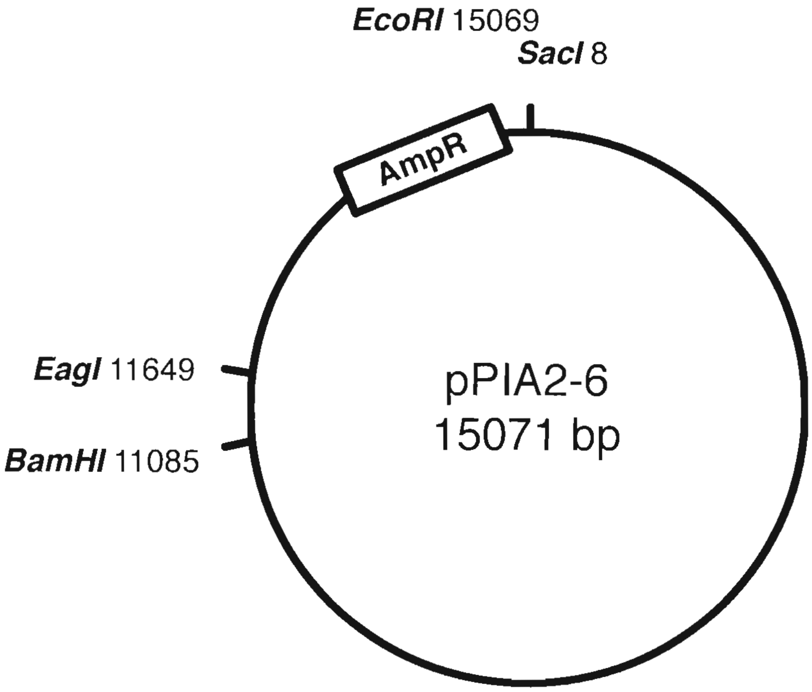

Figure 3.3: A restriction digest map of the cutting sites used in this thesis for pPIA2-6. The amp resistance gene is highlighted.

The DNA used in these experiments comes from a plasmid called pPIA2-6, a gift from the Bustamante Lab at UC Berkeley [18]. It is a $15\,kb$ circular plasmid with a gene for ampicillin resistance and numerous unique restriction endonuclease sites, shown in Figure 3.3. In an *E. coli* host, the ampicillin resistance gene allows for selecting only those cells which contain the pPIA2-6 plasmid in liquid cultures and on agar plates containing ampicillin. Large amounts of our plasmid of interest can then be harvested from the ampicillin-resistant cells through a plasmid preparation.

To modify the DNA for single-molecule stretching experiments, we need to differentially label opposite ends of a linearised fragment so that each end can bind to a different bead. To do this, the DNA is incubated with the restriction endonucleases *EagI* and *EcoRI* which bind to specific sequences along the DNA and cut the backbone (hence "nuclease"). In the case of *EagI* and *EcoRI*, these are at sites 11649 and 15069, which leaves two linearised fragments of lengths $11.651\,kb$ and $3.42\,kb$. The endonucleases used leave sticky

EagI	***EcoRI***
5' ... C 3' ... GCCGG	5' ... G 3' ... CTTAA

Figure 3.4: The sticky overhangs generated on the ends of a $12kb$ piece of pPIA2-6 DNA after a double digest with *EagI* and *EcoRI*. As *EagI* leaves only unpaired Cs and Gs, while *EcoRI* has unpaired As and Ts, differential labeling using bio-dCTPs and dig-dUTPs (which will bind in place of a dTTP) along with dGTP and dATP, is a single straightforward reaction.

ends, shown in Figure 3.4. With a nucleotide length of $0.338nm/bp$, the $11.651kb$ DNA has a contour length of $3.94\mu m$.

EagI and *EcoRI* were chosen specifically for the nucleotide composition of the sticky ends generated by nuclease cleavage. Sticky ends may be filled in using a DNA polymerase and chemically modified deoxynucleotides, in particular bio-dCTP (Invitrogen) and dig-dUTP (Roche) along with unmodified dNTPs. Purified by gel extraction (QIAGEN QIAEX II), $20\mu g$ of the $12kb$ $Eag-Eco$ fragment, $10\mu L$ of $1mM$ of each dNTP and 5 units of Klenow exo- polymerase fragment (Fermentas) were added in a $1\times$ REact 3 buffer (Invitrogen), and kept at $37°C$ for thirty minutes. The polymerase activity was inactivated by the addition of $5\mu L$ of $0.5M$ EDTA (pH 8.0). The DNA was then purified from excess dNTPs and enzyme (QIAEX II), and resuspended in TE buffer. Each end of this DNA now contains two copies of either a dig-labeled or biotinylated nucleotide, which can interact with the anti-dig and streptavidin coated beads, and the differential labeling prevents both ends of the DNA binding to a single bead.

Prior to injection into the optical tweezers chamber for a single-molecule experiment, the labeled DNA is incubated on a shaker at room temperature for one hour with $2.17\mu m$ anti-dig beads at a ratio of 100 molecules per bead. This ratio has been empirically determined to give a high probability for tethering a *single* molecule between beads in the instrument. A lower concentration of DNA leads to rare tethering events, while a higher concentration leads to multiple-molecule tethers, making data analysis difficult.

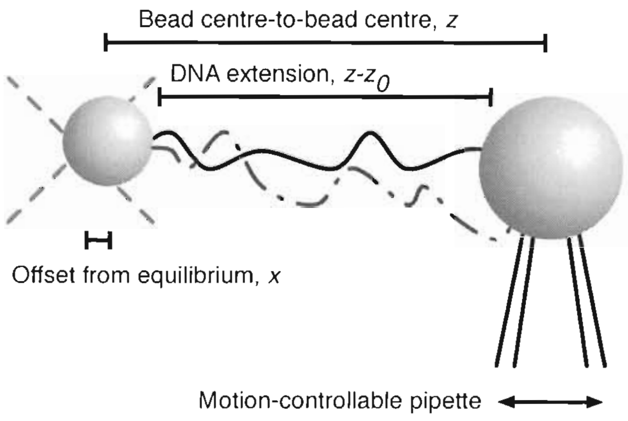

Figure 3.5: Schematic of the force-extension experiment. A DNA molecule tethered between two beads is pulled taut and relaxed by the motion of the micropipette bead via computer or manual control. Experimental variables measured in this process are the bead centre-to-bead centre distance, and the offset of the trapped bead from the trap centre. The optical trap stiffness is determined prior to tethering the DNA. An off-axis DNA tether is shown as a dashed line.

3.2.2 Force-extension curves

To actually carry out a force-extension experiment, streptavidin-coated beads are introduced into the trapping chamber, where one is grabbed via suction to the tip of the micropipette. Anti-dig beads which have been incubated with DNA for one hour as described above are then introduced via a syringe into the pressure-controlled flow system detailed in Chapter 2. After trapping an anti-dig bead and calibrating the optical trap constant (see Chapter 2), an automated "fishing" algorithm moves the streptavidin bead held on the micropipette toward and away from the trapped anti-dig bead, waiting for evidence of a tether between the two. When a tether forms, the trapped anti-dig bead is displaced from the trap centre as the streptavidin bead is pulled away. From this point on, either automatic or manual control of the pipette position and simultaneous measurement of the two bead positions via the edge detection algorithm gives enough information to construct a force-extension curve for the tethered DNA. A schematic of the experiment is shown in Figure 3.5.

When attempting to fit the data obtained from these experiments, the actual DNA extension is *not* measured. Instead, the extension data is contained within the bead centre measurements, and the radii of the beads must be subtracted. Another ambiguity in the data arises because of the bead held by suction to tip of the micropipette. While the trapped bead is free to re-orient in the trap such that the DNA is tethered on-axis with the micropipette bead, the micropipette bead is not free to do this same re-orientation. As such, the DNA may be bound off-axis (as shown by a dashed line in Figure 3.5), which will lead to a shorter than expected maximum extension of the DNA at high force. There is no way of knowing where the DNA is bound, so a dummy variable which takes into account both the bead radii and binding site mismatch is introduced to the WLC model. Letting z be the measured centre-to-centre data, z_0 is then this offset parameter. Rewriting Equation 3.6,

$$F = \frac{k_B T}{L_p}\left(\frac{1}{4(1-(z-z_0)/L_0)^2} - \frac{1}{4} + \frac{z-z_0}{L_0}\right), \tag{3.9}$$

where all the other variables are the same as before, we are free to leave z_0 and L_p as the fitting parameters. For this DNA, $L_0 = 3.94\mu m$ is known.

An example of the low-force fit to Equation 3.9 is shown in Figure 3.6, where the force-extension data were obtained in a buffer of $150 mM$ NaCl, $10 mM$ Tris, $1 mM$ EDTA, pH 8.0. Previous measurements in this buffer [19] yielded a persistence length value of $L_p = 53\ nm$. The fit from Figure 3.6 gives a value of $L_p = 52.0nm$ and an offset parameter $z_0 = 2.22\mu m$. This offset parameter is smaller than the sum of the two bead radii ($2.61\mu m$), implying an off-centre binding site for the micropipette bead. Fits from eight $F-z$ curves on three molecules gives a persistence length of $L_p = 52.1 \pm 0.6 nm$ (mean $\pm$ standard error), all in agreement with previous measurements in this buffer.

It is clear from the inset of Figure 3.6 that the standard WLC does not fit the data at high force. Data from $5\,pN < F < 30\,pN$ is shown in Figure 3.7, with the associated fit from Equation 3.8, the Odijk relation. The fit gives a persistence length $L_p = 52.7 \pm 0.5 nm$, in good agreement with previous measurements. The K_0 parameter is higher than measured in other buffers, at $K_0 = 1656 \pm 3\,pN$ ($\approx 10\%$ higher than previously reported values), however this particular buffer has not been used for high-force fitting before. The corresponding inextensible WLC with a persistence length fixed at $53 nm$ is shown as a dashed line, clearly not fitting the high force data and showing the necessity of incorporating an enthalpic term.

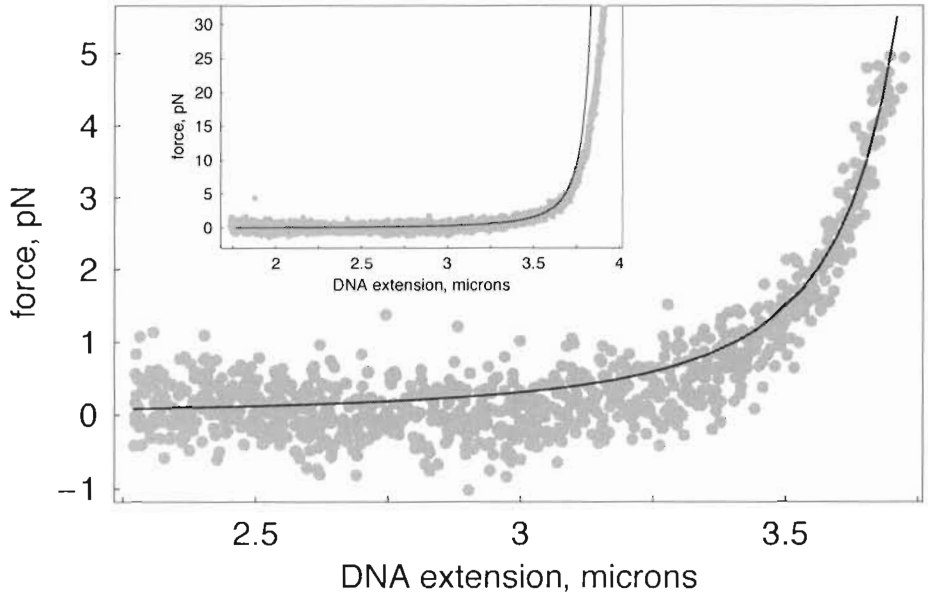

Figure 3.6: DNA force-extension data and the associated fit to low ($F < 5\,pN$) force by the standard WLC (Equation 3.9). Good agreement between theory and experiment is evident, with some deviation from the data at intermediate forces ($F \approx 0.1\,pN$) as expected. The fit yields a persistence length $L_p = 52.0nm$ and an extension offset $z_0 = 2.22\mu m$. **Inset**–high force data shows the standard WLC model is incapable of capturing the elasticity above $\sim 5\,pN$ with these fit parameters.

3.3 Sub-elastic chains

While the WLC models are in good agreement with the data from optical trapping experiments, a new set of measurements on DNA adhered to a surface and imaged via atomic force microscopy has cast into doubt the quadratic dependence of the elastic energy on bend stiffness. Wiggins *et al.* used high-resolution AFM images to trace the DNA backbone adhered to a mica surface [20]. They observed spontaneous, large angular bending of the DNA chain at a much higher frequency than predicted by the WLC model. As such, a new model for DNA was devised called the sub-elastic chain. An energy function of the form

$$\frac{E}{k_B T} = \alpha|\theta|, \tag{3.10}$$

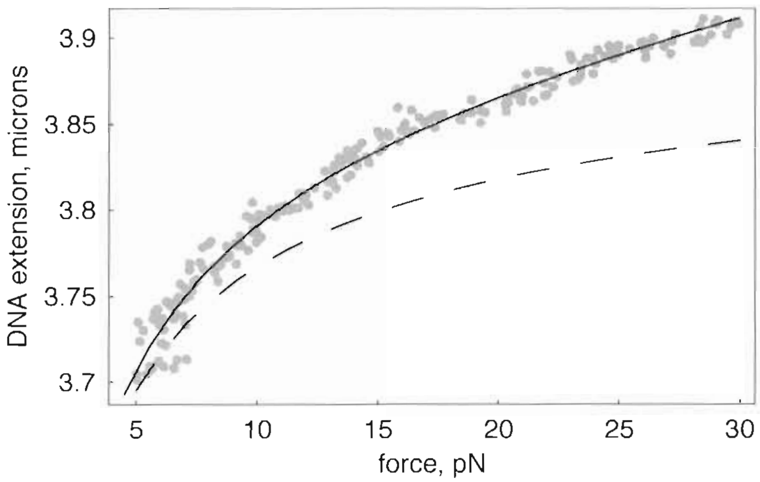

Figure 3.7: High force ($5\,pN < F < 30\,pN$), yielding a persistence length $L_p = 52.7 \pm 0.5\,nm$ and a stretch modulus $K_0 = 1656 \pm 3\,pN$. This value is larger than previously reported [16], but the buffer conditions are slightly different than used in previous studies. The standard WLC fit is shown as a dashed line, and completely misses the high-force data.

where α is a dimensionless constant that depends on the length scales being measured was used to fit the data. This results in a much lower energy build up at higher bend angles θ, which may be important as it is thought that many enzymes and even histone proteins require DNA to be in a highly bent state for proper cellular function. Direct measurements of θ are not possible in an optical-trapping instrument, so while the WLC models fail to agree with the frequency of high angular deviations observed in these AFM experiments, they are still useful models when studying polymers through their force-extension relations.

Chapter 4

Haemophilus influenzae and DNA uptake

4.1 *Haemophilus influenzae*

Haemophilus influenzae is a Gram-negative bacteria that resides in the upper respiratory tract of higher organisms, including humans. It was mistakenly attributed to be the cause of the common flu by Dr. Richard Pfieffer during an influenza pandemic in 1890, but this was simply coincidental as *H. influenzae* is commonly found in healthy humans. It is, however, responsible for a number of other illnesses, including bacteremia and bacterial meningitis, particularly in infants [21]. *H. influenzae* cells are roughly a micron long and 300-400 nanometres in diameter, as seen in our microscope.

Haemophilus, literally "loves heme", requires a prefactor to heme in its environment to live. In the laboratory it is most often grown on chocolate agar plates with additions of hemin and the growth factor nicotinamide-adenine dinucleotide, nutrients which are naturally available in our respiratory tracts. It has a relatively small genome (slightly less than 1.9 Megabase in length), and because of this it was the first free-living organism to have the entirety of its genome sequenced [22], slightly ahead of *E. coli*.

H. influenzae is also naturally competent to take up DNA from its environment. Why a cell has evolved this ability is still hotly contested, but three mutually non-exclusive reasons have been identified [23]. First, this could be a way to acquire new genes. By taking up DNA, a cell may use this new genetic material to gain new traits, such as resistance to an antibiotic. A second possibility is to use external DNA for repair, particularly if the DNA taken up comes from a closely related organism. A third reason is the use of the DNA as a food source [24], for elements such as phosphorous, carbon, and nitrogen, or even simply for free nucleotides. If the pool of free nucleotides in the cell is depleted, a replication fork can stall while waiting for the appropriate nucleotide, which can prove fatal if the cell begins to divide before DNA replication is complete.

As all three options are useful to a cell, any are plausible candidates for the evolutionary reason for the development of DNA uptake in bacteria. It is perhaps useful to look at the environment under which cells become competent in the first place. For *Haemophilus influenzae*, competence is most easily induced in the laboratory when the cells are placed in a starvation medium such as MIV [25]. MIV lacks nucleotide precursors and sugars[1], and in this medium the regulatory proteins CRP and Sxy induce expression of competence genes, leading to the formation of uptake complexes. The cells become competent within approximately 30 minutes (during which time competence genes are transcribed), and remain competent for two to three hours in MIV. That the cells become competent when starved of sugars and nucleotides may implicate the food-source theory, but it does not rule out the possibility of other ways to induce competence in *H. influenzae*.

4.1.1 DNA uptake machinery & the Uptake Signaling Sequence

In becoming competent, dozens of genes all regulated by CRP and Sxy are activated, leading to the translation of many different proteins, all thought to be involved with the DNA uptake complex. In other species (*B. subtilis*, *N. gonorrhoeae*) most of the proteins involved have been determined, but in *H. influenzae*, the set of proteins assumed to be translocases (the enzymes involved in translocation of DNA across the membranes) is unknown. Proteins involved with uptake which are known are components of a pseudopilus, and are orthologues to the type IV pili or type II secretion systems that are well known from other bacteria. These include the traffic NTPase PilB, pseudopilin protein PilA, a membrane protein PilC, and a secretin ComE [23]. The actual DNA recognition, binding, and channel proteins have not been identified.

A further complexity of DNA uptake by *H. influenzae* is its sequence specificity. Early

---

[1] MIV contains (all amounts in $\mu g/mL$ excepts salts in mM): Arg, 21; Asp, 4032; Cys, 6; Glu, 314; Leu, 61; Lys, 35; Met, 18; Ser, 65, Tyr, 42; Ile, 33; Gly, 2.5; His, 13; Val, 35; Phe, 46; Thr, 20; Ala, 48; Pro, 50; fumarate, 1000; citrulline, 12; Tween-80, 200; NaCl, 80; $MgSO_4$, 1; $CaCl_2$, 1.3; KH_2PO_4 12.8.

studies on DNA uptake by *H. influenzae* showed that an 8.1 *kb* section of *H. influenzae*'s own genome was efficiently taken up, but other DNA (a vector derived from *E. coli*, in this case) was not [26]. A restriction endonuclease map of the DNA that was readily internalised by *H. influenzae* implied that there were as many as 600 "uptake sites" present in the genome, and that the recognition sites themselves are "perhaps 8-12 base pairs long" [26]. Since this pioneering work, we now know that the recognition site or USS (for uptake signaling sequence) is a nine-base-pair motif, 5'-AAGTGCGGT-3', that is highly over-represented in the *H. influenzae* genome [23]. While this sequence appears necessary for efficient uptake, no candidate protein has been identified that might be responsible for sequence recognition. It is also possible that a sequence-independent mechanism is involved with uptake, such as high local kinking of the DNA [27], as a highly local kink may be required to initiate entrance in a small channel protein in the outer membrane. If it is indeed a deformation of the DNA which leads to binding and uptake, there should be a family of sequences that have relatively low energetic costs to kink. There are experiments ongoing to determine how much deviation from the "perfect" USS can be tolerated and still observe efficient uptake [28].

While the way *H. influenzae* recognises only specific sequences for uptake is still unclear, a general mechanism for DNA uptake from other bacteria may help explain the overall mechanism in *H. influenzae*. *N. gonorrhoeae* is another Gram-negative bacteria which is capable of DNA uptake, and it too requires a USS for efficient DNA uptake. A schematic of the type IV pili and uptake machinery is shown in Figure 4.1, much of which is homologous to proteins in *H. influenzae*. Components used in the type IV pili system such as the secretins and a pilus-like assembly are found in the uptake complex, where disassembly of the pseudopilus is implied in initial uptake across the outer membrane and into the periplasm.

This is relevant to uptake by *H. influenzae* because in both cases the pseudopilus genes are expressed, and the general structure involving secretins and an inner membrane pore or motor is common to both organisms. However, there are some important differences. The most significant of these are blebs called "transformasomes", implicated in the DNA uptake process in *Haemophilus*, which are membranous structures thought to envelop DNA and protect it during transport across the cell wall [29]. As well, while the pseudopilus proteins are needed for DNA uptake by *Haemophilus influenzae*, there are no large filamentous structures which extend beyond the outer membrane, as are found in *N. gonorrhoeae*. Because of this, and because of the need to identify the translocase proteins, much is left to discover about the *H. influenzae* uptake complex.

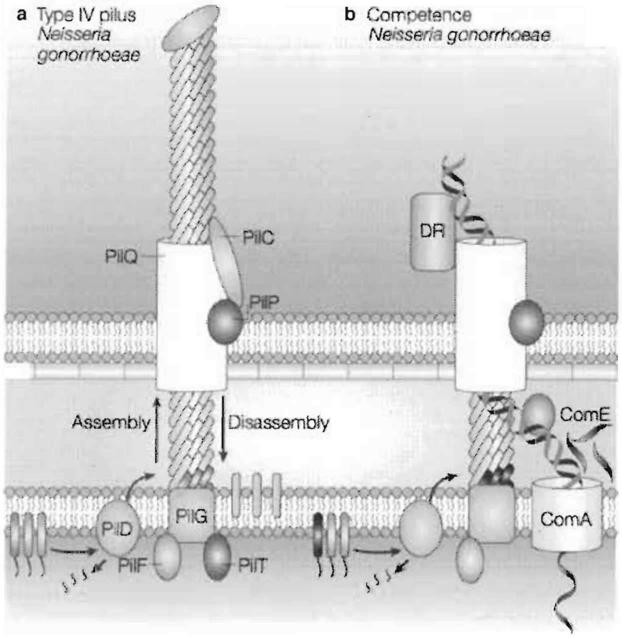

Figure 4.1: Similarities between **a** the type IV pilus and **b** the uptake mechanism in *N. gonnorhoeae*. In type IV pili, the pilus crosses both membranes, goes through the secretin PilQ which interacts with the pilot protein PilP. In the case of the competence machinery, a DNA recognition protein (DR, yet to be discovered) lies at the tip of a secretin to bind DNA with the appropriate sequence. A periplasmic protein ComE helps deliver the DNA to ComA, a cytoplasmic membrane protein, through which the DNA enters the cytoplasm. Used with permission from D. Dubnau, from [23].

4.2 The uptake machinery as a molecular motor: measurable physical quantities

The disassembly of a pseudopilus has been implicated in the *N. gonnorhoeae* uptake process, transporting DNA across the outer cell wall. *H. influenzae* is also known to have an active transport mechanism in its outer membrane, as there are mutant strains which close the inner membrane to DNA transport, leaving DNA stuck in the periplasm between the inner and outer membranes [30, 31]. That the uptake complex contains at least one molecular motor means a variety of interesting measurements on the *Physics* of the system can be studied. A previous study on DNA uptake by the bacterium *B. subtilis* [32] will be used as inspiration for experimentation on *H. influenzae*. Because of the Gram-negative nature of *H. influenzae*, and the sequence-specificity in DNA binding and uptake, the experiments outlined below will give valuable insight into the mechanism of *H. influenzae* DNA uptake.

4.2.1 Linear uptake measurements

The most straightforward experiments of DNA uptake at the single-molecule level involve linear uptake with a USS positioned near the free end of DNA, making it easier for the USS to find the binding site on the cell via diffusion in the optical tweezers instrument. A schematic of this kind of experiment is shown in Figure 4.2, where the DNA of interest is attached to a bead held in the optical trap, and a competent *H. influenzae* cell is immobilised to the surface of a bead held on the tip of the micropipette. This assay allows measurement of a number of interesting physical parameters, including dispersion in the uptake kinetics as a function of force, searching for a possible stall force for the uptake motor, testing the energy source of the complex, looking for cooperativity among the inner and outer membrane machinery, and finally testing the efficiency of uptake with respect to the USS orientation.

Kinetic studies are very straightforward: using the optical tweezers as a force clamp, it is possible to measure the bead to pipette position as a function of time, watching the tether length between the two decrease. This kind of measurement yields uptake rates at a constant force, which can be repeated at a number of forces to similarly probe the force-velocity relation, testing for load-dependent uptake rates. Another means to test load dependence is

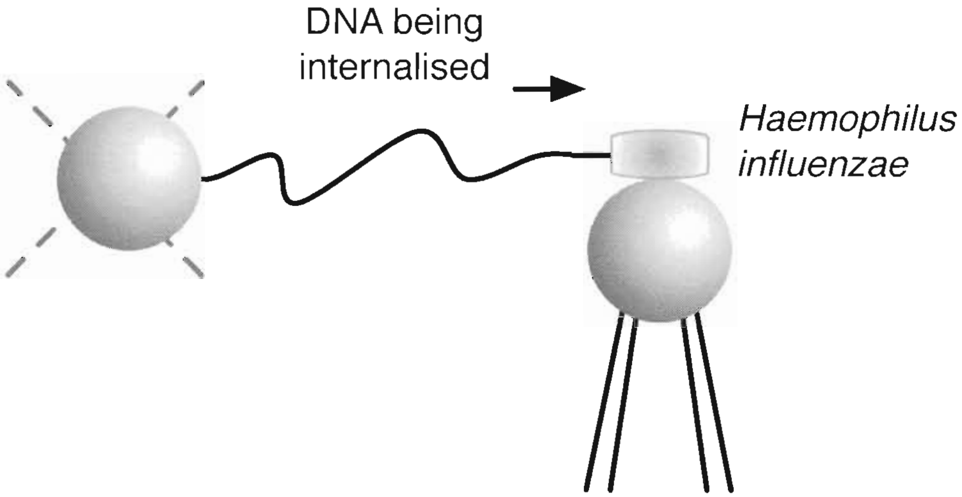

Figure 4.2: Experimental geometry for linear uptake measurements, allowing measurement of force-velocity curves, stall forces, and the energy source of the motor. With the cell immobilised to the surface of a bead held in the micropipette, a linear strand of DNA containing a USS near the free end is presented to the cell for binding and subsequent uptake. Upon binding and the initiation of uptake, tracking the position of the optically trapped bead relative to cell will give information on the uptake process.

to leave the pipette at a constant position, allowing the cell to "pull" the bead out of the trap centre as it is taking up DNA. This gives a quick measure of the load-dependent kinetics, but if there are other dynamics involved (pausing or slipping along the DNA template) it will be difficult to determine the force-velocity relationship, given that the translocation rate for other related motor proteins is quite fast [32, 33]. These measurements would give clues to the underlying enzyme kinetics: no load-dependence of the uptake kinetics would imply that the rate-limiting step in the reaction mechanism is not the force-generating step.

These experiments can also test for the stall force of the uptake machinery. The stall force for many other enzymes is quite low ($< 7\,pN$ for kinesins, $< 25\,pN$ for RNA polymerase [2]), but *B. subtilis* was able to take up DNA without any load-dependent velocity up to $40\,pN$ [32]. (The optical tweezers described in Chapter 2 can exert forces up to $\approx 60\,pN$). Another DNA translocase, the ϕ29 phage motor also continues to function under very high load (measured stall force = $57\,pN$ [33]), so comparisons between these and the *H. influen-*

zae machinery will be interesting, particularly to determine whether there is a general trend in the strength of DNA translocases.

The energy source for the uptake machinery in *H. influenzae* can also be tested, as in the work with *B. subtilis* by using proton uncouplers to reduce the proton gradient across the membrane [32]. This was found to be sufficient to stop uptake in *B. subtilis*, which can also be readily tested with the inner membrane of *H. influenzae*. Unfortunately, it is not possible to discount other energy sources (such as ATP in the cellular milieu) as being co-requirements for DNA uptake. Changing the ATP concentration is a technique often used when studying recombinant, purified molecular motors *in vitro*, but this experimental variable is not an option when working with a living cell without seriously disrupting the normal cellular activity.

That the uptake complex spans two membranes means there are two separate channels through which the DNA must be transported. It isn't known whether the inner membrane has simply an open pore or an active molecular motor, but there are mutants (mutations to either *rec2* or *comF* [30, 31]) which are still able to bind and take up DNA across the outer membrane, but which are no longer able to move DNA across the inner membrane, leaving DNA stuck in the periplasm. If there is indeed active transport across the inner membrane in wildtype *H. influenzae*, then comparing the uptake kinetics between wildtype and the inner membrane mutants is a way to measure any cooperativity between the inner and outer membrane transport proteins. Much has been said about cooperativity of transport theoretically (e.g. [34]), but measurements of *in vivo* dynamics are difficult to obtain.

Finally, changing the orientation of the USS at the end of a free piece of DNA allows testing of the orientation dependence of binding and uptake. As the USS is asymmetric it is reasonable to believe that efficient binding and uptake is also asymmetric, so determining the probability of binding and initiating uptake as a function of USS orientation and comparing slight mutations in the USS sequence can also help determine what exactly the recognition mechanism might be.

4.2.2 Testing uptake directionality

In addition to the linear uptake directionality measurements described above, a more complicated assay is also able to probe the response of the cell to a USS buried in the middle of a long piece of DNA. The two most readily obvious possibilities are that the cell either binds DNA and initiates uptake along a single direction, leaving the strand "upstream" from the USS untouched, or that DNA is internalised from both directions simultaneously. Determining the uptake mechanism from bulk studies is challenging. A single-molecule assay could determine the directionality of the uptake process if both ends of the DNA could be tracked at all times. A so-called "three-bead assay" gives this possibility, shown in Figure 4.3.

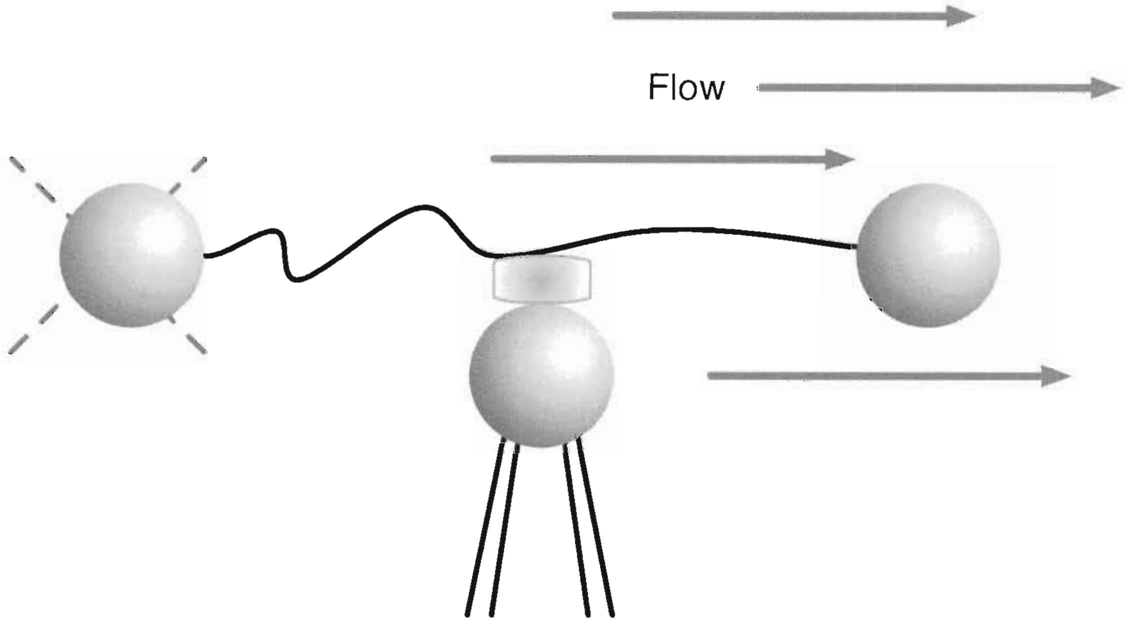

Figure 4.3: Experimental geometry for a proposed "three-bead assay", useful for determining linear vs bi-directional uptake. With the cell immobilised to the surface of a bead held in the micropipette, both ends of a linear strand of DNA containing a USS in the centre of the sequence are bound to distinguishable beads (for identifying orientation). Upon binding and the initiation of uptake, tracking the positions of both beads relative to cell will give information of the uptake process.

By tracking both beads connected to a single piece of DNA with the USS buried in the middle, it would be possible to study the uptake directionality directly. It is unknown whether both sides of the DNA are internalised at the same time, or if only one side is taken up during the process, and how the orientation of the USS affects uptake. Can the uptake complex accommodate first one side of the DNA, and then the other? Is there any nuclease activity if only one strand is taken up? The proposed three-bead assay will give significant insight into the molecular workings of the uptake process in *H. influenzae*.

Chapter 5

Toward single-molecule DNA uptake

To carry out the experiments detailed in the previous chapter, we require an optical trap, DNA containing a USS which can be labeled for uptake measurements (similar to the labeling for force-extension experiments detailed in Chapter 3), and we need to immobilise cells on a surface. Since the optical trap is discussed and characterised in Chapter 2, this chapter details the creation of a new DNA plasmid for uptake measurements and attempts to immobilise cells on beads.

5.1 pPIU1: A new plasmid for DNA uptake measurements

The basic requirement for carrying out single-molecule uptake measurements is an appropriate molecule of DNA to "feed" a *Haemophilus influenzae* cell. Instrument limitations, the most significant of which is the time required to determine whether the DNA is bound and being internalised by the cell, must also be accounted for. Similar to dsDNA "fishing", repeated back and forth motion to determine if tethering between the DNA and immobilised cell occurred is necessary and can take many seconds. While the actual uptake rate for *H. influenzae* is unknown, the ϕ29 phage packaging machinery translocates at a rate of $100\,bp/s$ [33] and *B. subtilis* takes up DNA at a rate also nearing $100\,bp/s$ [32]. Both required the use of a long molecule of DNA for sufficiently long uptake times. For single-molecule experiments with *H. influenzae*, a new DNA plasmid containing a USS was created called pPIU1, approximately $14\,kb$ in length.

5.1.1 Digestions, extractions, ligations

Two plasmids were combined to create pPIU1: pPIA2-6, detailed previously in Chapter 3 (see Figure 3.3), and a $3\,kb$ plasmid called pUSS1 (so named for the presence of the nine base pair USS, itself created by inserting the USS sequence into the *SmaI* site of pGEM-7Zf(+) vector [35]). Figure 5.1 shows the restriction endonuclease map for unique cutters of pGEM-7Zf(+), which are unchanged with the addition of the USS except to remove the *SmaI* site.

To incorporate the USS into a long plasmid, pUSS1 was cut with the restriction endonucleases *SacI* and *BamHI*. This linearises the plasmid and removes $13\,bp$ of sequence. pPIA2-6 was then digested with the same two enzymes, giving strands of lengths $11\,kb$ and $4\,kb$. By running both digests on a 0.7% agarose gel, three of the four distinct segments can be separated (while the $13\,bp$ strand migrates much too fast, and contains far too little DNA, to be visualised). Purifying the $11\,kb$ segment from pPIA2-6 and the $3\,kb$ segment from pUSS1 by gel extraction (QIAGEN QIAEX II DNA extraction kit), one obtains the two peices of DNA with complementary 5' overhangs, which can be re-circularised to form a new plasmid.

This recircularisation is faciliated by T4 DNA Ligase. For the two segments to form a single plasmid, the backbone of both segments must be covalently linked. DNA ligases act on the 3' hydroxyl end of one strand and the 5' phosphate group on a second strand, and form a covalent phosphodiester bond between them [36]. This chemically links the two strands together.

If both digestions went to completion, there are at least three possible plasmids which may be formed upon ligation: first, the joining of the $3\,kb$ pUSS1 fragment and $11\,kb$ pPIA2-6 fragment, second, two pPIA2-6 fragments joining together, and third, the joining of two pUSS1 fragments. However, the *BamHI* and *SacI* sites on pUSS1 were separated by only $13\,bp$, and there is no way to distinguish single digestion (linearisation) from a double digest. If any of the pUSS1 plasmids were only linearised, the addition of a ligase will lead to recircularised pUSS1 as well. To eliminate the possibility of re-ligation of singly digested pUSS1, Antarctic phosphatase (New England Biolabs) was used to remove the 5' phosphate groups from the pUSS1 digestion products. This modification makes self-ligation of pUSS1 impossible assuming the phosphatase reaction goes to completion, and

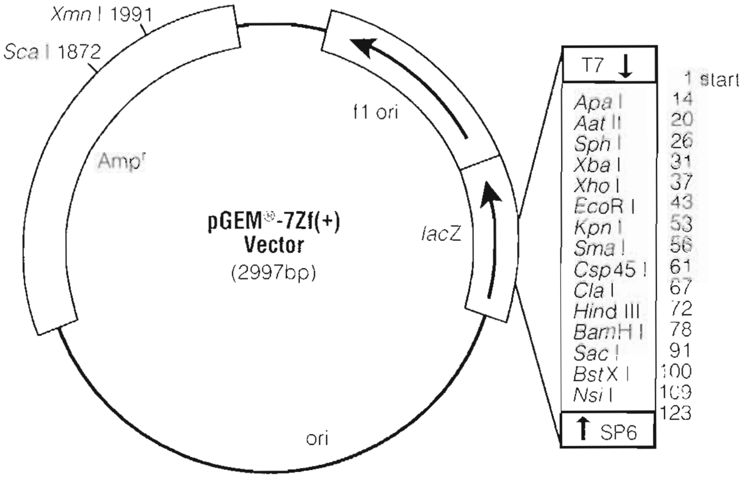

Figure 5.1: Unique restriction digest map for pGEM7Zf(+). A $200bp$ sequence including a USS inserted at the *SmaI* site creates pUSS1. From [35].

also removes the possibility of two separate pUSS1 fragments forming a plasmid as well. Creating a plasmid from two pPIA2-6 fragments will still occur, however analysis of the plasmid map from Chapter 3 shows that the AmpR gene has been cut out and purified away, while a pUSS1+pPIA2-6 fragment still contains the AmpR gene. As in Chapter 3, media containing ampicillin will be used to ensure only the pUSS1+pPIA2-6 plasmid is selected for. The plasmid formed by two pPIA2-6 fragments will be ignored for this reason in the rest of the treatment.

5.1.2 Transformations, harvests

To create large amounts of this DNA, it is necessary to transform a cell line with this new plasmid. As the workhorse of molecular biology, *E. coli* is again used as the host organism for generating lots of plasmid DNA.

Transformations with *E. coli* are different from *H. influenzae*'s natural transformation abilities. *E. coli* is not capable of naturally taking up DNA, so the cells must be specially prepared for the procedure.

A number of standard protocols exist for transformations [36], and the typical strain

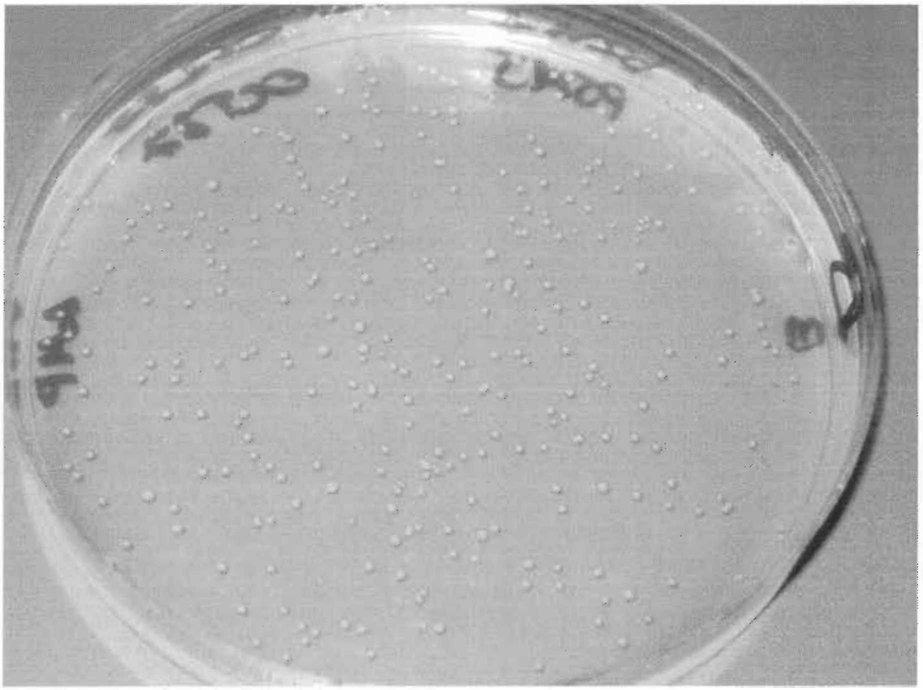

Figure 5.2: Colonies of *E. coli* cells after a successful transformation of pPIU1.

of host *E. coli* used is DH5α. The protocol followed is that of "chemically-induced competence", as in Reference 27. DH5α cells (at a concentration of $10^9/mL$) are initially suspended in a solution of ice cold $CaCl_2$ ($500\mu L$ total volume), making them 'chemically competent', or more susceptible to the transformation procedure. After adding $20ng$ of plasmid, the cells and DNA are left to incubate, on ice, for 30-45 minutes. After incubation, the cells are placed in a heat bath at $42°C$ for no more than 60 seconds, after which LB broth at $37°C$ is added. Being left on a shaker in an incubator at $37°C$ for 1.5-2 hours allows the cells that survived the heat shock to begin expressing the transformed plasmid's genes – in the case of pPIU1, they will begin to express the AmpR gene, giving resistance to the ampicillin. Plating $100\mu L$ of the cell solution on an LB agar plate containing $50mg/mL$ ampicillin will then select for only those cells which survived the heat shock and were transformed with the plasmid. If the cells were properly transformed, the agar plate appears dotted with little colonies as in Figure 5.2 after an overnight incubation.

A colony is the product of a single cell having survived and divided over many generations. A single colony is picked and used for large-scale liquid cultures, allowing harvesting of upwards of a milligram of DNA by large scale "maxi preps" from one litre culture volumes. Such an amount of DNA would last for months of single-molecule experimentation.

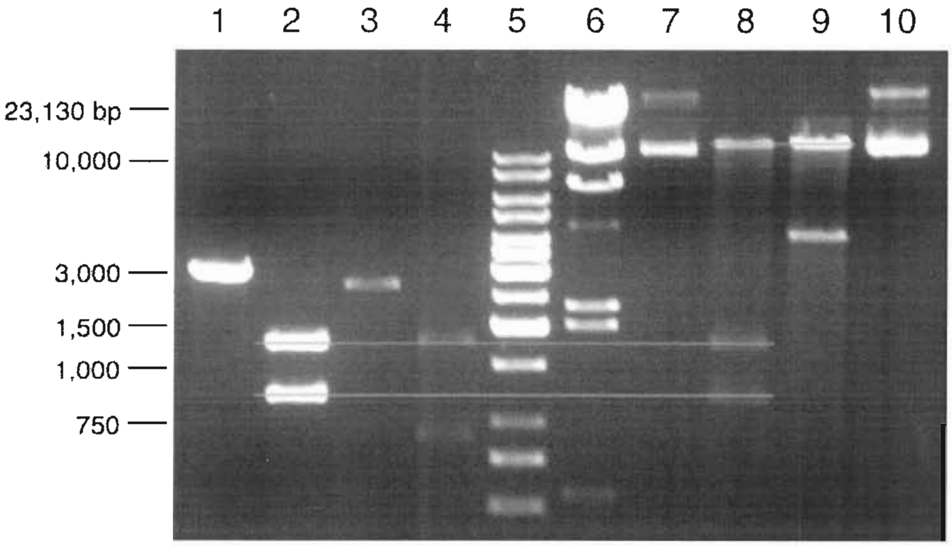

Figure 5.3: Agarose gel (0.7%) showing the digestion of pPIU1 components and their sources. Lane 1 contains uncut pUSS1, while lane 2 contains digested (with *BamHI*, *SacI*, and *ScaI*) pUSS1. Lanes 5 and 6 contain a 1*kb* ladder (Fermentas) and $\lambda/HindIII$ fragments, respectively. In lane 7 is uncut pPIU1, with its triple digest in lane 8. Lane 10 contains uncut pPIA2-6, with its double digest in lane 9. The main result is shown by the guides to the eye: pPIU1 is a combination of a section of pUSS1 (containing the USS, shown digested in lane 2) that is 3*kb* in length, and a section of pPIA2-6 that is 11*kb* in length. Lanes 3 and 4 contain an undesired, shorter ligation and transformation product, which is not relevant to the creation of pPIU1.

Plasmid preparations ("mini preps") were carried out on five of the colonies obtained as a result of transformation. Of these, one appeared to be recircularisation of pUSS1, a second contained a plasmid which appeared to be a shortened pUSS1, possibly created by digestion and ligation of pUSS1 in the cell, while the other three contained the desired products. Examples of the DNA obtained from transformed colonies are shown in Figure 5.3, where the restriction enzymes *BamHI*, *SacI*, and *ScaI* were used to digest the product

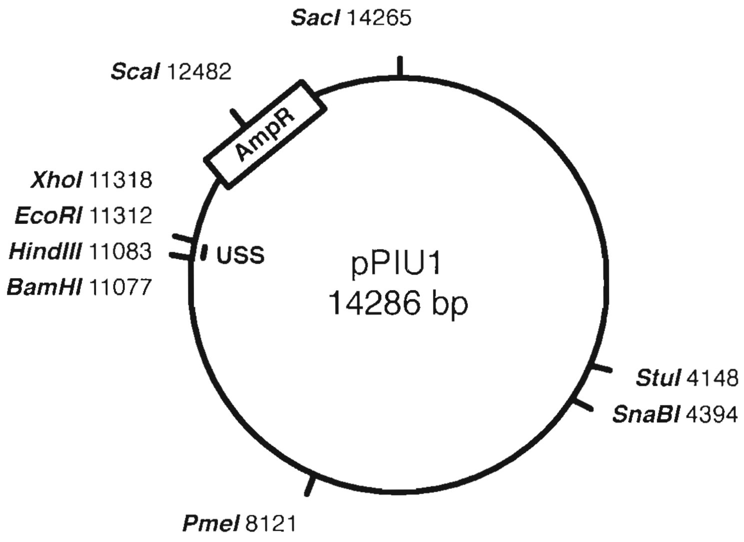

Figure 5.4: Restriction digest map with some of the unique restriction sites for pPIU1. The USS is located around position 11200.

plasmids. A double digest of *BamHI* and *SacI* should display the $3kb$ and $11kb$ segments described above, and the addition of *ScaI* will further cut the 3kb segment into two strands each below $2kb$ in length. This is indeed what was observed, showing that the ligation reaction created the desired plasmid, in lanes 7 and 8.

5.1.3 pPIU1 plasmid map

The plasmid map of pPIU1 shown in Figure 5.4 gives details of the unique restriction sites available for linearisation and labeling. The USS is in the centre of a $221bp$ sequence starting at position 11103, leaving restriction enzyme sites on either side to create both the forward and reverse orientation of the USS for uptake experiments. Other pairs of enzymes (chosen in the 3000-5000bp range) allow for a USS at the centre of the DNA for experiments to probe uptake polarity.

5.2 Cell immobilisation

To measure single-molecule uptake events with sufficiently high spatial resolution (*nm*), the cells themselves must be anchored to a surface. As the surfaces of different cell strains are highly variable, there is no one solution for specifically immobilising cells to a surface, however a number of different options are available. The simplest method takes advantage of non-specific interactions between the complex surface of a cell and uncoated polystyrene beads or coverslip surfaces. Coating beads or surfaces with mucin, a protein found in *H. influenzae*'s environment is also a promising avenue. Finally, a more complicated method is to specifically target proteins on the cell surface via antibodies. All three methods were attempted.

5.2.1 Non-specific interactions

Polystyrene beads with many different surface coatings are used in optical trapping experiments. My experiments so far (see Chapter 3) have made use of carboxy-terminated and anti-digoxigenin- and streptavidin-coated beads. I will make use of protein-G coated beads in the next section. All of these beads were tested for their ability to bind competent *H. influenzae* cells. Between 1 to $10 \mu L$ of cells at a concentration of $10^9/mL$ were incubated with $1 \mu L$ of 5% w/v beads of each variety on a shaker for one hour. This gave ratios of 1 to 10 cells per bead in a volume of $11\ \mu L$. Upon dilution into $1 mL$ total volume of MIV (see section 4.1), the cells were observed under both our optical trap acting as a light microscope and a phase contrast microscope, in the Redfield laboratory. In no situation did I observe any cells bound to beads. In an attempt to force a higher amount of interaction in our tweezers instrument, beads suctioned to the tip of the pipette were 'squished' into cells held briefly in the optical trap. Upon closing the laser shutter, the cells were seen to simply diffuse away, implying no attachment between the cells and beads. This occurred for all bead types described above. In separate experiments involving the phase contrast microscope, all cells were seen diffusing rapidly due to Brownian motion, with no cells seen absorbed to a coverslip surface.

5.2.2 Mucin

Mucins are glycoproteins [37] found in mucus secreted by epithelial cells. There are more than 10 mucin genes found in humans, and the common structural motif is that of a hydrophobic peptide backbone connected to oligosaccharide (carbohydrate) chains. As the major component of mucus, mucins form large aggregates which help give mucus its consistency.

However, as mucus (and therefore mucin) is found in the respiratory tract of higher organisms, *H. influenzae* may be able to bind (or non-specifically stick) to a mucin-coated surface. To this end, attempts to crosslink mucin to Protein G-coated polystyrene beads were made using a standard protocol [38].

Perhaps not surprisingly, with mucins in a liquid medium a very mucus-like viscosity dominates. Any attempt at spinning down a bead/mucin solution resulted in a very thick mucus-like liquid and no sign of any beads, having become inseparable from the mucosal mess.

5.2.3 Antibodies

Another promising approach to immobilising cells to a surface is to use antibodies directed to outer membrane proteins (OMPs). Creating antibodies is a long process involving the inoculation of rabbits (or another animal host) with *H. influenzae* cells, letting the animals create antibodies against the invading cells, and then bleeding the rabbits to collect a serum containing the antibodies. As an alternative to creating antibodies here, Professor Bob Munson from Ohio State University kindly sent us a gift of antibodies (raised in rabbit) directed to both proteins "P2" and "P5", OMPs that make up the majority of the surface proteins by mass [39, 40]. These antibodies were raised against a different strain of *H. influenzae* (type b), but the proteins P2 and P5 are thought to be conserved in the strain we are using (Rd). The Smith lab from the University of Washington also sent antibodies directed to P4, but after negative results were obtained in control experiments, it is believed that these are mislabeled. I do not discuss anti-P4 any further.

Both types of sera were then used to coat Protein G-coated polystyrene beads [38]. Protein G weakly recognises antibodies, and a cross-linking agent is able to further stabilize protein G-antibody binding. To $50\mu L$ of 5% w/v Protein G-coated beads, $10\mu L$ of sera and

$3\mu L$ of crosslinking buffer were added and left shaking for one hour. These beads were then washed in PBS (pH 7.4) and resuspended in $60\mu L$ of pH 6.5 PBS solution. Dot blots were used to assay antibody binding.

Dot blots [36] are a relatively quick and easy way to determine whether proteins of interest are present. To assay the crosslinking of antibodies to beads, both types of antibody beads were compared to protein G beads and carboxy-terminated beads (as negative controls) for the presence of antibody. After wetting a PVDF membrane (Pierce, 88518) with methanol and TBS buffer, the membrane was "dotted" with $1\mu L$ amounts of each bead type in three serial dilutions: 5% w/v, 0.5% w/v, and 0.05% w/v. After letting the dotted liquid absorb, the rest of the surface was "blocked" with a solution containing the protein bovine serum albumin (BSA), rendering the rest of the surface of the membrane covered with protein and unable to give spurious signal when assaying for antibodies. With the surface blocked by BSA, a secondary antibody specific to antibodies generated by rabbits (Promega, S3731) is introduced (1:5000 dilution by volume in TBS-Tween buffer), about $10mL$ total volume. These secondary anti-rabbit antibodies are chemically modified to fluoresce in the presence of the reagent "Western Blue" (Promega, S3841). After adding $2mL$ of Western Blue atop the membrane and incubating for 10 minutes in the dark, if fluorescence is observed, antibodies created by a rabbit are present.

Figure 5.5 shows the results of the dot blot experiment, each row containing a single bead type with the concentration shown at the top of the figure. Both the anti-P2- and anti-P5-coated beads show a strong blue signal, indicating the presence of antibodies from rabbits that are indeed coating the beads. Comparing the anti-P2 and anti-P5 dots to those of the protein-G-coated beads, a greater than ten-fold stronger intensity is observed. The carboxy-terminated beads are unable to bind to the secondary antibody at all.

To test whether the antibodies are able to bind to the surface of the *H. influenzae* cells, another set of dot blot experiments was performed. Dilutions of live, competent cells were dotted on PVDF membranes and then exposed to the same antibody serum used to coat the beads above. After washing, the secondary antibody solution is introduced to again look for the presence of anti-P2 or anti-P5 on the cells. Figure 5.6 shows the result of these experiments, which clearly demonstrates that the secondary antibody specific to rabbit antibodies is present in the dotted areas and that the secondary anti-rabbit antibodies themselves are not responsible for the observed signal.

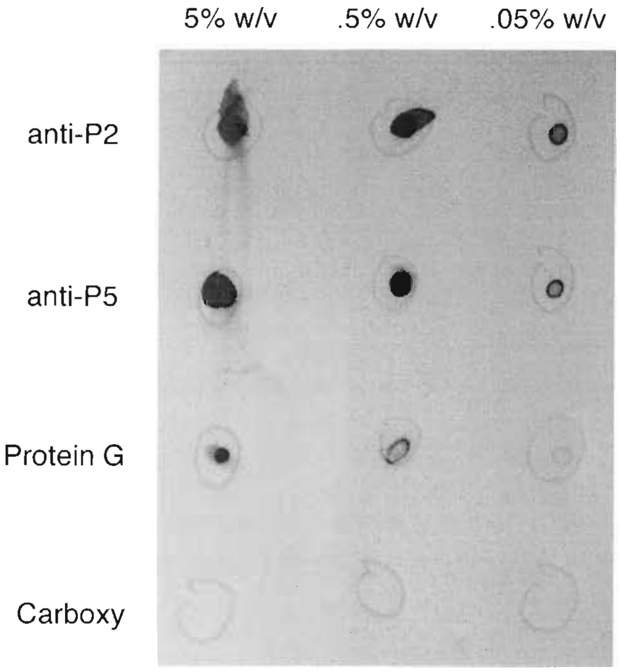

Figure 5.5: Dot blot assays for antibody-labelled beads. Anti-P2- and anti-P5-coated beads give a signal more than an order of magnitude larger than the protein-G-coated beads, signifying that anti-P2 and -P5 are in fact present on the bead surfaces. Carboxy-terminated beads show no sign of antibody, as expected.

With the confirmation that the beads are coated by our antibodies of interest and that the antibody sera binds to our cells, attempts were made to immobilise cells to the bead surfaces. High concentrations of beads and cells (10^9 cells/mL and 5% w/v beads) in low volumes ($10\mu L$ total) were left incubating for 1 hour and observed under a light microscope. No cells were seen immobilised on a bead surface (hundreds of beads observed), despite the high concentrations of both cells and beads and the long incubation times.

A more direct method of attempting cell to bead attachments involved using the micropipette and the optical tweezers. Using suction, antibody coated beads were repeatedly brought into direct contact with cells held in the optical trap. Again, no binding events were observed, despite direct contact between the bead and cell surfaces for extended (30-60 seconds) periods of time. Transient events were observed regularly, but cells and beads would

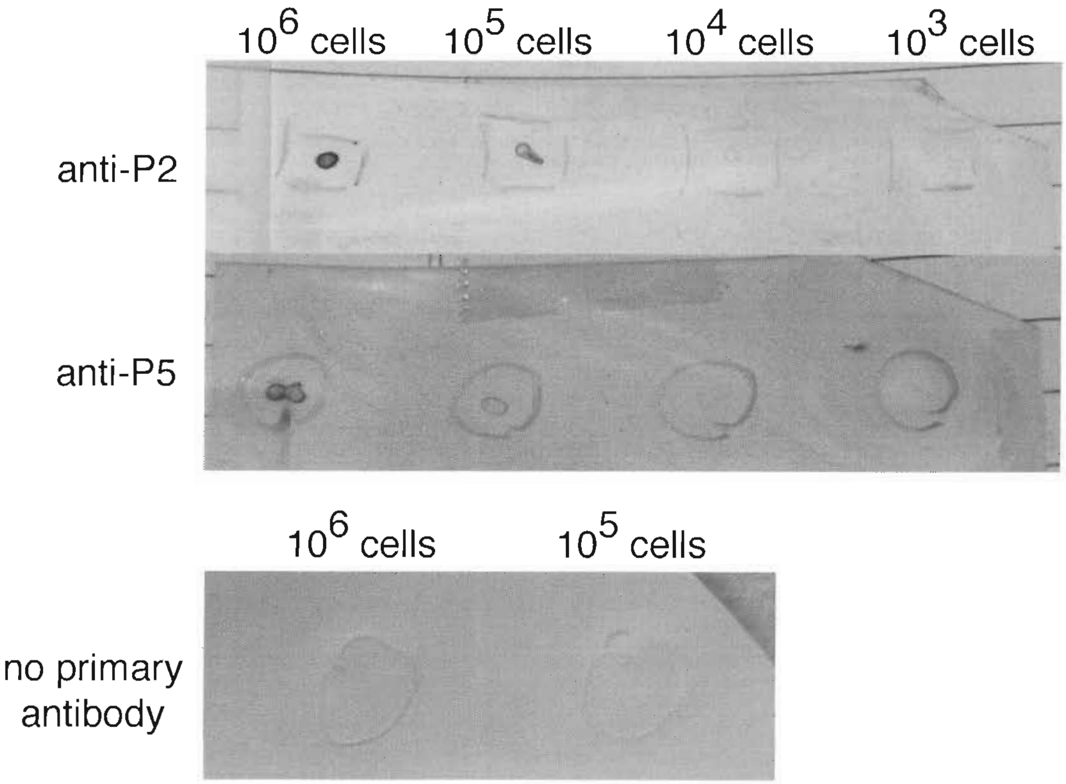

Figure 5.6: Dot blot experiments showing the binding of anti-P2 and anti-P5 to the surface of competent *H. influenzae* cells. The control experiment involving no primary antibodies below shows that the signal is indeed obtained only in the presence of anti-P2 or anti-P5 sera.

quickly diffuse apart. As previous experiments involving antibodies have been shown to bind with forces up to 60 *pN* [33], this diffusion apart could not occur if the complexes are properly bound.

It is also possible to suction cells directly to the pipette, however, unlike the polystyrene beads, the cell surface is irregular and in my experience does not form a good seal with our pipette tip. This results in residual suction which draws other bacteria or beads to the pipette, rendering force measurements extremely difficult. Alternative methods of immobilisation could involve modifying the pipette puller to produce narrower tips, or fabricating pipettes with more sophisticated methods (e.g. an ion beam). I have not explored these options.

5.2.4 Analysis & further possibilities

Determining why no binding between beads and cells was observed is not clear. The dot blot experiments quite clearly show interactions between both cells and the antibody sera, and that the protein-G beads are also coated with proteins from the sera. One possibility is that the serum obtained from an innoculated rabbit contains a wide variety of antibodies and other molecules found in the bloodstream, and the number of antibodies directed toward P2 and P5 may be only a small fraction of these. Since the secondary anti-rabbit antibody will bind to many different proteins from rabbit, it is unclear how many antibodies of interest end up coating our beads. Another possibility is that the antibody interactions are negated in MIV. Dot blot experiments in MIV will show whether the buffer conditions are critical for antibody/surface protein recognition.

While the above methods were unsuccessful in immobilising *H. influenzae* cells to the surfaces of beads, there are further avenues to pursue. One possibility is to create antibodies to the exact strain used in single-molecule uptake experiments, which would involve infecting rabbits with our cells and harvesting serum from them after innoculation. The strain against which the anti-P2 and anti-P5 antibodies were created is *H. influenzae* type b, from sick humans. Growing antibodies against our specific strain (Rd) may be more successful, as the conservation of protein sequence between *Haemophilus* strains is unknown (though assumed high). Growing antibodies against our strain in particular bypasses these issues. This is a long process, and while facilities are in place to infect rabbits and harvest antibodies, there may be alternatives. One possibility is to exploit and modify membrane proteins already found on the surface of *H. influenzae*. A recent paper [41] reported selective biotinylation of a membrane channel protein in oocytes, enabling attachment to neutravidin-coated beads. This is a more direct means of attaching to a cellular surface, and it does not require an outside source of antibodies, but is unfortunately a very complicated procedure.

Chapter 6

Conclusions

This thesis has presented work toward studying the DNA uptake process by *H. influenzae* at the single-molecule level. In order to do so, a single-beam optical tweezers instrument was constructed, characterised, and used to measure the elasticity of single double-stranded DNA molecules. Molecular biology techniques were then used to construct a new plasmid, pPIU1, suitable for both linear uptake measurements and determining the polarity of uptake in a three-bead assay.

To carry out these experiments, competent *H. influenzae* cells immobilised to a surface were required. Non-specific interactions between cells and coverslip surfaces, cells and polystyrene beads, and cells and antibody-coated polystyrene beads were tested as a means of immobilisation, but under no circumstances were cells seen to attach specifically to any of the aforementioned surfaces. Lacking the ability to immobilise cells, uptake measurements involving high resolution force and position measurement were not possible. Further suggestions for immobilising *H. influenzae* cells to surfaces were discussed.

Bibliography

[1] C. Bustamante. Unfolding single RNA molecules: bridging the gap between equilibrium and non-equilibrium statistical thermodynamics. *Quarterly Reviews of Biophysics*, pages 1–11, 2006.

[2] C. Bustamante, Y.R. Chemla, N.R. Forde, and D. Izhaky. Mechanical Processes in Biochemistry. *Annual Review of Biochemistry*, 73:705–748, 2004.

[3] M.T. Woodside, P.C. Anthony, W.M. Behnke-Parks, K. Larizadeh, D. Herschlag, and S.M. Block. Direct measurement of the full, sequence-dependent folding landscape of a nucleic acid. *Science*, 314:1001–1004, 2006.

[4] C. Cecconi, E.A. Shank, C. Bustamante, and S. Marqusee. Direct observation of the three-state folding of a single protein molecule. *Science*, 23:2057–2060, 2005.

[5] D. Collin, F. Ritort, C. Jarzynski, S.B. Smith, I. Tinoco, and C. Bustamante. Verification of the Crooks fluctuation theorem and recovery of RNA folding free energies. *Nature*, 437:231–234, 2005.

[6] A. Ashkin. Optical trapping and manipulation of neutral particles using lasers. *Proceedings of the National Academy of Sciences*, 94:4853–4860, 1997.

[7] K. C. Neuman and S.M. Block. Optical trapping. *Review of Scientific Instruments*, 75:2787–2809, 2004.

[8] A. Rohrbach. Stiffness of Optical Traps: Quantitative Agreement between Experiment and Electromagnetic Theory. *Physical Review Letters*, 95:168102, 2005.

[9] G. J. L. Wuite, R.J. Davenport, A. Rappaport, and C. Bustamante. An Integrated Laser Trap/Flow Control Video Microscope for the Study of Single Biomolecules. *Biophysical Journal*, 79:1155–1167, 2000.

[10] K.C. Neuman, E.H. Chadd, G.F. Liou, K. Bergman, and S.M. Block. Characterization of photodamage to Escherichia coli in optical traps. *Biophysical Journal*, 77:2656–2663, 1999.

[11] K. Berg-Sorensen and H. Flyvbjerg. Power spectrum analysis for optical tweezers. *Review of Scientific Instruments*, 75:594–612, 2004.

[12] Yi Deng. Calibration and characterization of static and modulated optical traps. Master's thesis, Simon Fraser University, 2007.

[13] C. Storm and P.C. Nelson. Theory of high-force DNA stretching and overstretching. *Physical Review E*, 67:051906, 2003.

[14] Paul J. Flory. *Statistical Mechanics of Chain Molecules*. Interscience, 1969.

[15] J.F. Marko and E.D. Siggia. Stretching DNA. *Macromolecules*, 28:8759–8770, 1995.

[16] M.D. Wang, H. Yin, R. Landick, J. Gelles, and S.M. Block. Stretching DNA with Optical Tweezers. *Biophysical Journal*, 72:1335–1346, 1997.

[17] T. Odijk. Stiff chains and filaments under tension. *Macromolecules*, 28:7016–7018, 1995.

[18] R.J. Davenport, G. J. Wuite, R. Landick, and C. Bustamante. Single-molecule study of transcriptional pausing and arrest by E. coli RNA polymerase. *Science*, 287:2497–2500, 2000.

[19] S. B. Smith, Y. Cui, and C. Bustamante. Overstretching B-DNA: The Elastic Response of Individual Double-Stranded and Single-Stranded DNA Molecules. *Science*, 271:795–799, 1996.

[20] P.A. Wiggins, T. van der Heijden, F. Moreno-Herrero, A. Spakowitz, R. Phillips, J. Widom, C. Dekker, and P.C. Nelson. High flexibility of DNA on short length scales probed by atomic force microscopy. *Nature Nanotechnology*, 1:137–141, 2006.

[21] Kenneth Todar. *Textbook of Bacteriology*. http://textbookofbacteriology.net/, January 2007.

[22] R.D. Fleischmann, M.D. Adams, O. White, R.A. Clayton, A.R. Kirkness, A.R. Kerlavage, C.J. Bult, J.F. Tomb, B.A. Dougherty, and J.M. et al. Merrick. Whole-genome random sequencing and assembly of Haemophilus influenzae Rd. *Science*, 269:496–512, 1995.

[23] I. Chen and D. Dubnau. DNA uptake during bacterial transformation. *Nature Reviews Microbiology*, 2:241–249, 2004.

[24] R. J. Redfield. Do bacteria have sex? *Nature Reviews Genetics*, 2:634–639, 2001.

[25] R.J. Redfield, A.D.S. Cameron, Q. Qian, J. Hinds, T.R. Ali, J.S. Kroll, and P.R. Langford. A Novel CRP-dependent Regulon Controls Expression of Competence Genes in Haemophilus influenzae. *Journal of Molecular Biology*, 347:735–747, 2005.

[26] K. L. Sisco and H.O. Smith. Sequence-specific dna uptake in haemophilus transformation. *Proceedings of the National Academy of Sciences*, 76:972–976, 1979.

[27] R.J. Redfield. 2006. Personal communication.

[28] L. Wilson. Personal communication, 2006.

[29] M.E. Kahn, F. Barany, and H.O. Smith. Transformasomes: Specialized Membranous Structures That Protect DNA During Haemophilus Transformation. *Proceedings of the National Academy of Sciences*, 80:6927–6931, 1983.

[30] T.G. Larson and S.H. Goodgal. Donor DNA processing is blocked by a mutation in the com101a locus of Haemophilus influenzae. *Journal of Bacteriology*, 174:3392–3394, 1992.

[31] R. Barouki and H.O. Smith. Reexamination of phenotypic defects in rec-1 and rec-2 mutants of Haemophilus influenzae Rd. *Journal of Bacteriology*, 163:629–634, 1985.

[32] B. Maier, I. Chen, D. Dubnau, and M. P. Sheetz. DNA transport into Bacillus subtilis requires proton motive force to generate large molecular forces. *Nature Structural & Molecular Biology*, 11:643–649, 2004.

[33] D.E. Smith, S.J. Tans, S.B. Smith, S. Grimes, D.L. Anderson, and C. Bustamante. The bacteriophage ϕ29 portal motor can package DNA against a large internal force. *Nature*, 413:748–752, 2001.

[34] S. Klumpp and R. Lipowsky. Cooperative cargo transport by several molecular motors. *PNAS*, 102:17284–17289, 2005.

[35] Promega. Technical Bulletin 48. 2004.

[36] J. Sambrook and D. Russell. *Molecular Cloning: A Laboratory Manual.* Cold Spring Habor Laboratory Press, 3rd edition, 2001.

[37] J. Perez-Vilar and R. L. Hill. *Encyclopedia of Biological Chemistry*, pages 758–764. Elsevier, 2004.

[38] Jan Liphardt. Molecular biology protocols: Beads/Protein G/Ab.

[39] R.S. Munson Jr. and D.M. Granoff. Purification and Partial Characterization of Outer Membrane Proteins P5 and P6 from Haemophilus influenzae Type b. *Infection and Immunity*, 49:544–549, 1985.

[40] R.S. Munson Jr., J.L. Shenep, Barenkamp S.J, and D.M. Granoff. Purification and Comparison of Outer Membrane Protein P2 from Haemophilus influenzae Type b Isolates. *Journal of Clinical Investigations*, 72:677–684, 1983.

[41] P. Gorostiza, F. Tombola, A. Verdaguer, S.B. Smith, and C. Bustamante. Molecular Handles for the Mechanical Manipulation of Single-Membrane Proteins in Living Cells. *IEEE Transactions of Nanobioscience*, 4:269–276, 2005.